ABSTRACT

Title of Dissertation:	An Investigation of 3D Printed Materials as Electrets Iain Michael Kierzewski, Doctor of Philosophy, 2024
Dissertation co-directed by:	Prof. Liangbing Hu, Materials Science & Engineering Department UMD Prof. Nathan Lazarus, University of Delaware

3D printing is proposed for creating, optimizing, and integrating novel electret materials and composites. Additive manufacturing techniques have moved from simple prototyping to heterogeneous structuring and integration and have begun fabricating multifunctional sensing and harvesting materials like piezoelectric polymers and composites. Electrets can be made out of a variety of materials and offer piezoelectric coefficients orders of magnitude higher than traditional ceramic and polymer piezoelectric materials without requiring specific crystalline phases.

Through this work, I will demonstrate the first completely 3D printed piezoelectric material using a commercially available FFF printer. I will be investigating the effects of additive manufacturing parameters such as extrusion temperature and infill on the electret properties of printed materials. Finally, I will study novel cheap and renewable materials and composites such as delignified wood cellulose for their potential electret capabilities.

AN INVESTIGATION OF 3D PRINTED MATERIALS AS ELECTRETS

by

Iain Michael Kierzewski

Dissertation submitted to the Faculty of the Graduate School of the
University of Maryland, College Park, in partial fulfillment
of the requirements for the degree of
Doctor of Philosophy
2024

Advisory Committee:
Professor Liangbing Hu, Chair
Professor Robert Briber
Professor Isobel Lloyd
Professor Nathan Lazarus, University of Delaware
Professor Teng Li, Dean's Representative

Acknowledgements

Thank you to my colleagues and mentors at the Army Research Laboratory for their help and guidance throughout both my career and my dissertation work.

Thank you to my loving friends and my family, who have supported me through all the challenges I have faced on my path.

And thank you to my wife Alyson, who has been a deeply caring partner to me these many years.

Table of Contents

This Table of Contents is automatically generated by MS Word, linked to the Heading formats used within the Chapter text.

Chapter 1: Background

What is an Electret?

Electrets are dielectric materials with a quasi-permanent stored charge. Charges are injected onto and within the material through a variety of means, where they are stabilized by energy traps, and further by the dielectric response of the dipoles within the material. The very first electrets were mixtures of waxes which were brought from a melted state down to a solid state under a large DC electric field [1] in the early 1920s. These samples demonstrated a persistent polarization that was not destroyed by "touching by Bunsen flame, exposure to X-rays, planning with a knife, washing with some solvents, &c" [2], which is to say that the effect could not be explained by simple static electricity which would have easily been discharged by these means. Scientists would learn through later decades of research that the polarization in these materials was a result of real space charges which were trapped within the material [3, 4]. The first demonstrated commercial use for electrets can be found in a 1964 patent for the electret microphone co-invented by Drs. Sessler and West, wherein a charged electret film of polytetrafluoroethylene (PTFE) suspended opposite a counter electrode with an air gap in the middle converts pressure waves from sound into electrical signals [5]. Electrets can be seen in a variety of other applications from sensing [6], energy harvesting at both micro and macro scales [7, 8], biometrics and health monitoring [9, 10], and many others. The electret effect is seen to be a more as a fundamental property of most real dielectrics than a unique property of a few materials, and can be seen across many materials both natural [11] and engineered [12]. Recent events have even highlighted an especially important application for electrets in N95 filtration

masks, where the charges stored within the filter fibers aid in trapping aerosols while minimizing the pressure drop, something that pure mechanical filters cannot do [13].

Electret materials can be separated into two main categories, namely solid/real-charge electrets, and porous or piezo/ferro-electrets. The first category describes simple electrets of solid dielectrics with space charges embedded onto their surface or within their bulk and represents the earliest-discovered and most ubiquitous electrets [14]. The primary necessities for an electret material are that they have a significantly high resistivity (typically 10^8 Ω·cm or greater) to prevent charge recombination or decay, and that they have traps that are deep enough to hold charge carriers such as electrons or ions [15]. Beyond these basic requirements, electret materials are chosen for their processability. In this regard, many electrets are made of thermoplastics (e.g. ABS, PP, PTFE) due to their high resistivities and their facile forming and processing capabilities. Besides polymers, electrets can be made from glasses (e.g. SiO2) [16, 17], ceramics (e.g. hydroxyapatite) [18], as well as composites thereof [19]. The electret effect can also be observed in natural materials like conch shell, whose hierarchical structuring provides many charge storage sites leading to extremely high polarization [11]. The typical charge density of these types of electrets range from 0.1-10 mC/m^2, primarily limited by the dielectric constant and dielectric strength of the electret material. For comparison, the highest charge density of the most common ferroelectrics like the polymer PDVF and the ceramic PZT is 10-100 mC/m^2 [1]. A summary of electret materials, properties, and processing methods covered in this literature review is shown in Table 1.

Table 1 Electrets throughout literature compared by their figures of merit, fabrication methods, pros, and cons.

Electret	Materials	Charge density σ [mC/m2]	Piezoelectric Coefficient [pC/N]	Fabrication Method(s)	Pros	Cons
Polymer Foams [20]	PP PET PEN	0.1-1.0	d33: 100-500 (2000 stacked)	Extrusion, gas expansion, biaxial stretching	Roll-roll processing	Random pores, requires stacking and packaging for devices
Tubular	FEP [21, 22]	0.2-0.3	50-175	Lamination	Facile	Simple tube shape pores only
MEMS	CYTOP [23]	1.5	none	Spin-coating, lithography, O2 plasma	Highest stability	Requires lithographic patterning and plasma etch, not piezoelectret
MEMS	SiO2 [24]	5-25	none	Thermal growth, lithography	High charge density, thermal stability	High temperature deposition/growth, humidity sensitive, not piezoelectret
MEMS	Parylene [25, 26]	3-4	none	CVD, lithography	Large-scale deposition possible	Requires lithographic patterning, not piezoelectret
Molded	PDMS+PTFE [27, 28]	1.25	d33: 1500-3500 d31: 235	Mold and stack, coat pores with PTFE	High sensitivity, stretchable	Humidity sensitive, 2D stacked pore structures only
3D printed mesh [29]	PP, PLA	2.4-3.9	d33: 300	FFF printing, assembly	High charge density	Requires assembly
PDMS center layer [30]	PP, PDMS	0.82	544	FFF printed mold, assembly	Increased piezo using compliant center layer	Multiple processing steps
3D printed onto bulk film [31]	PLA, ECOFLEX, TPU	-	229 (TPU) 713 (Ecoflex)	FFF printed layers, elastomer outer layers, assembly	Elastomer outer layers shown to increase piezo	Requires thermal bonding of layers, additional assembly to reach full piezo
Vertically 3D printed [32]	PP, PLA	0.25 (PP) 0.12 (PLA)	Up to 800	Vertically printed tubular pores	Smoother surfaces, smaller pore and solid layers, no assembly	Small pores lead to drop off of d33 with bias force
My work 3D Printed [33]	ABS	0.3-0.6	d33: 80-100	FFF printing	Complexity, integrability, multi-scale (µm-mm)	Low throughput, requires further study

Despite the low charge density when compared with ferroelectric materials, the surface potential of these electrets can easily exceed 1000 V as their dielectric constant is low, making them especially useful for thin film applications in micro electro-mechanical systems (MEMS) [34]. The polymer electrets are attractive alternatives to SiO_2 or ceramics [17] due to their ease of processibility, though their temperature stability is a point of study for optimization [25].

The latter category (porous electrets) contains pores within the polymer where the charge is deposited. Piezoelectrets were first theorized around 1970 as charged polymers with

mechanically and electrically inhomogeneous layers which could result in a piezoelectric effect [35]. This effect was initially demonstrated in charged materials with two different polymer layers [36], where the softer of the two polymers would undergo greater strain, breaking the symmetry of the stack, and thereby a change in net polarization. Eventually this concept was integrated with that of the electret air-gap transducer in the form of the first internally porous PP films with charged voids [37]. The porous electret – once charged – contains charges of opposite polarity on the pore walls, forming large, engineered dipoles. It has been demonstrated that these artificial dipoles can switch their polarization depending on the poling field (i.e. ferroelectrets) and that they will change their polarization in response to strain (i.e. piezoelectrets) [35], as shown in Figure 1.

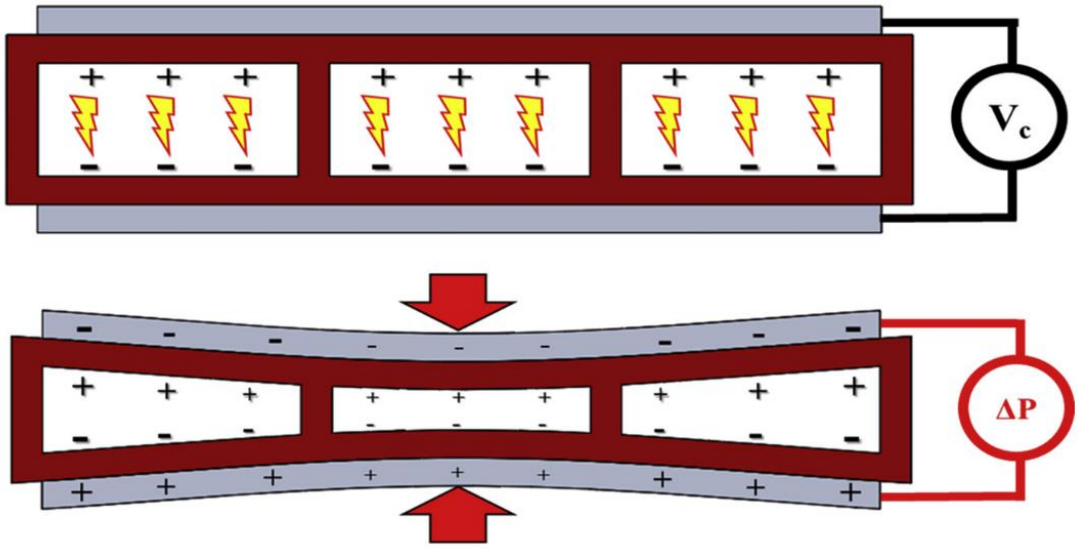

Figure 1 Direct charging (above) and effective piezoelectric effect (below) of a piezoelectret, from [33]

In the case of these porous ferroelectrets, the charges are created by the dielectric breakdown of the air within the pores, which follows the Townsend model of Paschen breakdown [38, 39]. The critical field (E_c) for breakdown is a function of the pore height d and

the pressure of the gas in the pore p, as shown in the equation below. A and B are constants based on the breakdown coefficients for the particular gas, typically air or nitrogen.

$$E_c = \frac{Ap}{B + \ln(pd)}$$

These charges are then deposited onto the walls of the pores, forming the artificial dipoles. As the material is strained, the dipole moment changes, and so the ferro/piezoelectret can exhibit an effective piezoelectric coefficient, making them useful as transducers. When compared with traditional polymer piezoelectrics like PVDF (d_{33} = -20 pC/N) and high performance ceramic piezoelectrics like PZT (d_{33} = 300-600 pC/N) [40], a very low elastic modulus allows the best piezoelectrets to have much higher piezoelectric coefficients (from 100's to 1000's of pC/N [6, 41]).

Approach

Electrets are charged using a variety of methods, the most common of which is corona discharge. The sample to be charged is placed on a ground electrode opposite a high voltage electrode in the form of a needle, array of needles, or a wire. The curvature in the high voltage electrode causes charge carriers to form (electrons for a negative potential, ions for a positive potential) and be accelerated towards the sample. A third electrode typically in the form of a grid can be imposed between the sample and the needle and biased at an intermediary potential. This grid electrode will more typically absorb or reflect charges at lower or higher potential (respectively), allowing for a more quantitative selection of the resultant surface potential of the charged electret [42]. Corona discharge can as well be used for porous ferro/piezoelectrets so long as the surface potential is high enough to cause subsequent Paschen breakdown within the pores [43].

To determine the dielectric properties of the electret material, the most frequently used and most powerful technique is dielectric spectroscopy. A small AC electric field is applied to the material across a range of frequencies, and the current is measured through the material. From this measurement, a variety of properties can be determined. The complex dielectric constant, loss tangent, and resistivity are the most important for an electret material. In addition, the presence and frequency of dielectric relaxations can be observed as peaks in the ε" spectrum and a large relative change in the ε'. In the case of pure polymers, these relaxations are the result of different polymer chain motions [44]. If the electret is a composite, there can be relaxations that are the result of the interface between the matrix (typically the polymer) and the additive, called the Maxwell-Wagner effect [45, 46]. In a charged piezoelectret, these relaxations can be indicative of different resonance modes of piezoactivity, allowing for simultaneous electrical and electro-mechanical characterization [47]. For crystalline or semi-crystalline polymers like polypropylene (PP), the crystallinity [48] and size of crystallites [49] will affect the electret's charge stability, with the interfaces between crystalline and amorphous regions providing additional trap sites for charge as well as affecting the glass transition temperature Tg which is related to the thermal stability of that charge [50]. The crystallinity or the percent of crystallization in a polymer is typically studied by differential scanning calorimetry (DSC) [51].

For an electret to be useful, it must hold its charge for anywhere from hours to decades, depending on the intended application. Eventually any electret will self-discharge as thermal energy causes the charges to escape their traps. Once the charge has escaped it will either hop to another trap, or the material's own finite conductivity will provide a pathway for it to reach ground or the edges of the material where it can combine with compensation charges from

humidity or particulates from the environment. Environmental processes such as moisture absorption will also add to this effect, further decreasing the charge stability in the electret [14]. There are a few methods for quantifying the charge lifetime of an electret. A simple and direct method is to measure the surface potential directly over time. To measure the surface charge or potential, the most direct method is to use an electrostatic voltmeter, which employs a vibrating electrode to normalize electric field in the test area under the probe and allow for accurate voltage measurement [52]. The measured voltage can be related to the charge through Gauss' law as applied to a parallel plate capacitor with charge density σ, relative dielectric constant of ε_r, and thickness d [34], as shown in the equation below.

$$VS = \sigma d \varepsilon_0 \varepsilon_r$$

This is a non-contact technique, which is important for measuring the potential from the electret without providing a path to ground which would either remove or compensate that charge. For electrets with shallower traps or higher conductivity, measurement times of hours or days may be sufficient to observe significant discharge. For more optimized electrets, however, the lifetime of the charges under ambient and low-temperature conditions will be too long to reasonably measure directly in this way. To that end, techniques such as thermally stimulated discharge current or voltage (TSDC/TSDV) are used. Herein, the electret is heated either to a constant elevated temperature or over a range of temperatures at a constant heating rate. The short-circuit current or the open-circuit voltage are measured as the electret is heated until eventually it is fully discharged. A typical TSDC curve is shown in Figure 3 of [53]. From this curve, two values can be extracted. The total charge density within the electret can be calculated by integrating the total discharged current over time, and the trap energy(ies) can be estimated

through an Arrhenius relation of the discharge peak temperatures as in [18]. Typically, deeper traps in an electret will relate to longer charge lifetimes as well as a more stable usable temperature range. For some polymer electrets, the interfaces between their crystalline and amorphous regions offer good trap sites, increasing the charge density within the electret [48]. To facilitate the formation of trap sites, additional phases are added to the matrix material such as ceramic or metallic particulates, which provides additional dielectric interfaces as well as promoting the growth of crystalline regions [45, 46].

In the case of the porous piezoelectrets, the internal charging behavior can be measured using a different technique. Ferro/piezoelectrets can also be charged by direct application of high voltage by electrodes. During the charging process, the current through the electret can be measured and integrated into charge. For a typical dielectric, this response looks linear. In a ferroelectret at fields above the critical field, a large current is drawn during the breakdown event, resulting in a large change in measured polarization. If the measurement is too slow then conductivity current will be integrated into the result, but for high resistivity sample and/or sufficient testing frequency, all measured charge in excess of the linear response can be attributed to charge generated by Paschen breakdown of the pores [54]. In analyzing these charge hysteresis loops, analogous terminology to ferroelectric testing is used. The “remnant polarization” in this case, or the charge after one polarity cycle remaining after the applied field returns to zero, will be the charge deposited within the ferroelectret. This represents a fundamental limit to the charge able to be stored in that ferroelectret; if the surface potential from the charge stored is sufficient to reach the critical voltage (in the opposite polarity) as the applied field is reduced, then this charge will neutralize destructively. Within ferroelectrets, this is seen

even as a “back-breakdown” effect in their charge hysteresis loops, where charge is formed in excess of the breakdown field of the air in the pores, leading to spontaneous breakdown in the reverse polarity of the applied field and a reduction in the total charge on the electret. Techniques have been studied to minimize this effect, from raising the temperature of the electret during poling [55] to infiltrating the electret with higher breakdown-coefficient gasses [56, 57]. Besides the charge stored within a ferro/piezoelectret, the effective piezoelectric charge coefficient (d_{xy}) is the primary figure of merit. Many of the porous piezoelectrets are anisotropic materials, so typically one of the values within the piezoelectric coefficient tensor (either d_{33} or d_{31}) are optimized at a time [28].

Electret Characterization Methods

Surface potential

The surface potential of an electret is typically measured using a non-contact probe such as a kelvin probe. Touching the surface of the electret would risk damaging it, discharging the stored charge, or transferring charges that would alter the charge density of the electret. In this work, a Trek 370 Electrostatic Voltmeter and Trek 347 non-contact probe was used to measure the surface potential of corona charged electret samples. Before each measurement, the probe fixture was adjusted with the tool off to the appropriate height for the sample to be measured. A sample surface-to-probe distance of 1mm was used to minimize external stray electric field effects and to provide accurate and repeatable locational measurements, based on a probe resolution chart provided by Trek. Then the tool was zeroed with the probe over a reference

ground. The probe was then maneuvered over the sample, and the voltage measured was read off and transcribed.

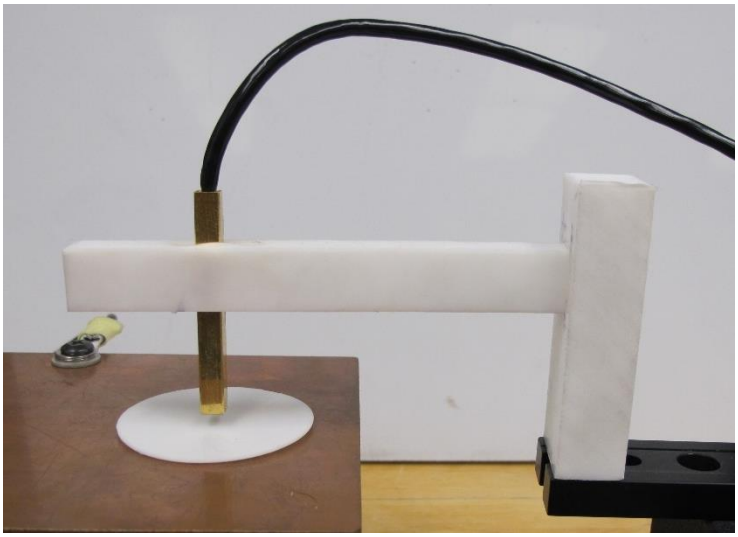

Figure 2 Electrostatic voltmeter probe and sample configuration for surface potential measurements

Effective Piezoelectric Constant

After a porous sample was charged, the effective piezoelectric constant in the thickness-wise or out-of-plane direction (d_{33}) was measured using a Berlincourt-type quasistatic meter from Poly-k Tech, shown below.

Figure 3 The Berlincourt-type quasistatic d33 meter was used to measure the piezoelectric coefficient for all porous samples.

This type of meter has two electrodes, one fixed and one that vibrates at a set frequency. The sample to be measured was clamped between the electrodes, and the thumb screw was tightened just enough to hold the sample in place without significantly deforming it. The clamping force was also confirmed using an in-line force transducer on the tool. The meter then calculates the d_{33} in pC/N by comparing the output signal from the sample with an internal reference PZT transducer. The measurement was repeated a minimum of three times at the same location on the sample, rotating the sample between measurements, and the average taken for each datapoint. Repeating the measurement in this way minimized the effects of slight errors in contact between the electrodes and the sample.

Dielectric spectroscopy

A Novocontrol Alpha Series was used for dielectric spectrometry measurements on solid coupons. The tool was initialized, and calibrations were run for open, short, and reference capacitance. Separate coupons were used for ambient/dry and temperature sweep measurements so as not to interfere with other measurements. Removable polished gold-plated electrodes were cleaned with ethanol before and after each test to reduce contamination between samples. Once cleaned, the electrodes were centered on the sample coupon and clamped into the test fixture. The fixture was then lowered into the test chamber. Dry nitrogen either from laboratory house nitrogen lines or from a liquid nitrogen dewar was kept running between measurements so that the test chamber was kept dry. "Ambient" samples were run without nitrogen.

The frequency for each sample was swept from $1x10^{-3}$Hz to $1x10^{7}$Hz. For temperature tests, the frequency was swept at 25ºC (room temp) first as a baseline, again at each elevated temperature, then finally at 25ºC again to see if there were any significant changes from baseline after the higher temps. Data was then analyzed and plotted using Matlab.

Differential Scanning Calorimetry (DSC)

Samples were taken from both un-printed filament and from printed coupons for DSC using a Perkin Elmer DSC 8500. All samples were stored in a dry box before use. Very small pieces were cut to fit the sample pans, weighed on a sub-mg scale, then crimped into the pan before loading into the tool. Three samples were repeated for each data point. Additional filament samples were run through two-cycle tests – the first cycle simulated the thermal effects of 3D extrusion, while the second cycle measures the "as-printed analogue" crystallinity.

Contributions

What will be demonstrated within this work is the capability of both cheaper 3D printers (e.g. Makerbot, Ultimaker) as well as newer high-resolution additive manufacturing tools (i.e. nScrypt, Nanoscribe) to directly print and precisely control both the structure of electret materials, measure their charge density and stability while simultaneously engineering their mechanical properties to maximize their piezoelectric sensitivity. The primary metrics for the materials in this study are the charge density (σ) and surface potential (Vs), the thickness-wise piezoelectric coefficient (d_{33}), and the charge stability measured as % of σ lost over time at ambient or at elevated temperatures.

The first contribution is the investigation of 3D printing filaments and resins, and the effects that printing and processing parameters have on the electret properties. There is currently a wealth of commercially-available materials for 3D printing. There is significant and growing interest in 3D printed electrets within the last few years, and an understanding of dielectric properties of 3D printing materials is key to electret study.

The second contribution is an investigation and demonstration of a MEMS-scale 3D printed porous electret. This technique could allow for far more complexity and vertical integration than current lithographically-defined electret materials. By utilizing a porous electret, it as well provides a possible alternative MEMS-scale piezoelectric material to traditional thin-film ceramic piezoelectrics.

The third contribution is the publication of the first completely 3D printed ferro/piezoelectret. This material was able to be 3D printed and then charged without any further

assembly, demonstrating the capability for FFF 3D printing to directly create piezoelectrets which could be later integrated directly into as-printed systems and devices.

The final contribution is the demonstration of ferroelectret charging in natural delignified wood material. The delignified wood material contains a pore structure that is far more uniform and well-aligned than the typical random-pore piezoelectret foams. It is as well a renewable material alternative to more expensive and environmentally harmful fluoropolymers.

Chapter 2: 3D Printed Electrets

Background

Piezoelectret research to date has largely focused on top-down processing approaches [58] such as film extrusion [59] followed by nucleation and expansion processes [60]. Such processes can result in films with very high piezoelectric sensitivity, but result in random pore size and distribution [6]. As well, these materials still require subsequent processing and packaging into multi-layer stacks to achieve the higher sensitivities reported and sufficient voltage outputs for energy harvesting [61]. Another fabrication method more recently investigated for piezoelectrets is the molding and thermal bonding of bulk films [21, 62]. The idealized structures generated using this technique are limited by the need to remove the template material from the electret after laminating and result only in very simple tubular pore structures. On the MEMS scale, electrets are typically patterned using lithographic processes [63], as well as mold-and-release piezoelectret structures, which can be repeated and stacked for thicker materials [10, 27], all of which are still layer-wise 2D techniques.

3D printing techniques have evolved past simple prototyping to allow for highly complex heterogeneous material fabrication. Materials with unique mechanical properties can be made using 3D printing that are not producible with other top-down methods [64]. Multiple materials can be integrated into the same tool, resulting in the ability to print full multifunctional devices [65]. The widescale accessibility of cheap 3D printers as well has allowed for ideas to be replicated quickly and easily between researchers and non-researchers. Consistent advances in 3D printers brings additional resolution, speed, and complexity to 3D printing. Newer MEMS-compatible nano-/micro-scale 3D printers such as the Nanoscribe could produce custom-

designed, well-aligned, porous electrets for long-term stable surface potential (biasing) as well as on-chip piezoelectric materials fabrication that does not necessitate high temperature annealing like traditional ferro/piezo-ceramics.

There have been some efforts to make use of additive technologies for creating piezoelectrets, but with important limitations. Layered mold-and-stack processes have been shown for poly-dimethylsiloxane (PDMS) electrets, where inkjet-based 3D printing was used to produce the molds to allow control over the resultant pore sizes, [66, 67] but these methods require significant additional steps beyond the 3D printing steps and do not take full advantage of 3D printing's ability to create complex 3D shapes. Many electrets are made from thermoplastics such as polypropylene (PP) and acrylonitrile butadiene styrene (ABS) due to their low dielectric loss and high formability, and their relatively low elastic modulus. As these materials are very frequently used in FFF 3D printing [68, 69], the ability of this process to create piezoelectrets is an obvious connection. FFF has indeed been demonstrated for use in creating assembling piezoelectret structures, wherein layers of ABS have been printed and subsequently thermal-bonded to create a porous sandwich structure [70, 71]. While these samples demonstrated measurable piezoelectret effect, they required significant post-3D printing steps and did not utilize bridging to create as-printed piezoelectrets. Another publication at the time [72] outlined the creation of a hydrophone using an FFF-printed PP layer, but without demonstrating designed pores, electrical charging, or electromechanical characterization of the resulting structure.

Since my publication, there has been continued research in the community on 3D printed electrets. Numerous publications have improved the d_{33} by optimizing the laminated construction

method [29], utilizing more compliant middle layers [30, 31], and even utilizing a vertical printing orientation to achieve thinner pore and polymer layers [32].

Motivation and Hypotheses

The goal in this portion of the work is to look into a number of widely-used 3D printing techniques to determine their feasibility in generating and optimizing electrets. FFF, SLA, 2PP, and direct extrusion techniques will be considered for their ability to generate well-defined porous structures at the size scale appropriate for Paschen-induced breakdown and charging. SLA and 2PP methods may be able to resolve features at the appropriate size scale, and generating open pores will be necessary for charging. FFF may struggle with generating open pores, though there are bridging parameters that can be used.

Sample Preparation

Fused-filament 3D printed electrets

The nScrypt 3Dn-500PF is a tool platform capable of CNC, extrusion, and FFF printing. Ruby nozzles are available for FFF printing head with very fine tip diameters, down to 50μm. In order to generate internal pores, an infill structure was utilized. Infill structures are typically utilized in 3D printing to minimize weight and material usage while still generating the desired shapes and minimally compromising strength of the printed part. Different slicer software will have different included infill patterns, but shapes such as triangle, square, and hexagon are commonly used. For this work, hexagonal infill structures were chosen as this infill shape was able to generate the largest pore spacing for a given infill percent. The infill percent is the measure of how much solid material is used for a given structure; lower infill percentages mean

larger pores, and vice versa. For the same filament material, lower infill percent samples were expected to have a lower effective Young's modulus in the thickness direction. The other anticipated factor for the effective Young's modulus is the thickness of the solid top and bottom layers above the middle infill region. Since d_{33} is inversely dependent on the effective Young's modulus of the piezoelectret, minimizing this property would lead to the maximum possible d_{33} for a given charge density and starting material.

Nine different series of infill piezoelectret samples were printed using different infill percents and layer thicknesses, as shown in Table 1Table 2. By changing the infill%, both the pore width w and the active area α were simultaneously altered.

Table 2 Summary of infill piezoelectret samples, geometric parameters, and charge densities. [33]

series	1a	1b	1c	2a	2b	2c	3a	3b	3c
infill %	20	10	5	20	10	5	20	10	5
w1 [mm]	1.53	1.79	7.24	1.55	5.14	7.8	1.8	2.33	7.72
w2 [mm]	1.87	2.01	7.62	1.96	5.74	8.15	2.2	2.71	8.77
α	0.82	0.89	0.95	0.79	0.89	0.96	0.82	0.86	0.88
1-α	0.18	0.11	0.05	0.21	0.11	0.04	0.18	0.14	0.12
thick [μm]	560	590	480	480	500	680	1170	680	1040
d1 [μm]	180	170	140	90	80	100	180	110	180
d3 [μm]	120	170	150	130	120	120	200	100	150
d2 min [μm]	100	70	50	110	110	230	660	340	530
d2 max [μm]	260	250	190	260	300	460	790	480	710
σ calc [mC m^{-2}]	0.29	0.27	0.28	0.35	0.39	0.40	0.46	0.55	0.47
σ meas [mC m^{-2}]	0.40	0.34	0.31	0.15	0.42	0.52	0.43	0.50	0.61

Nanoscribe

The Nanoscribe is a micro-scale 3D printer that utilizes 2-photon polymerization (2PP) to cross-link the monomer resin within a 0.6x0.6x3.3µm voxel size (using a 25x objective). 2PP technology is similar to SLA, but has much finer resolution at the cost of slower overall write times. The tool then rasters back and forth for each printed layer before adjusting the focus out of plane to print the next layer. Unlike an FDM printer, the Nanoscribe optics are submerged into the monomer resin while printing, as the focal distance from the tip of the optic is very small. As well, the Nanoscribe operates in an inverted orientation: a droplet of the highly viscous monomer resin is adhered to the printing substrate (diced silicon die of approx. 25x25mm), loaded into the printer upside down, and the optic is raised into the droplet and focuses on the substrate before beginning the print.

The samples are designed in Solidworks and exported as a dxf file; similar to the process for the FDM printers. The dxf file represents only a 280x280µm “chunk”, as this is the maximum movement distance of the fine-resolution stage controllers on the Nanoscribe. For prints larger than this chunk size, the less-precise piezo stage movement is used to move between chunks, so prints larger than one chunk must be split into chunks and repeated to generate a larger sample. The minimum size required for surface potential measurements was 6x6mm, as the probe for the surface potentiometer is 5x5mm, and the measured spot size is proportional to the distance between the probe tip and the sample. The smallest reasonable distance that the sample could be loaded under the probe was ~1mm, and a probe sample area of 6x6mm was determined by the surface probe manual. Each such sample took approximately 5hrs to print chunk-wise on the Nanoscribe. To maximize efficient use of the Nanoscribe alongside other

users in the clean room, samples were typically prepared in batches of 3-5 overnight or over weekend prints whenever possible. A few solid and porous samples were printed for comparison.

Other investigated techniques

Two other printers were investigated for use in generating porous electret samples but were ultimately not successful in generating samples with appropriate dimensions capable of being charged with the 10kV power supply available.

An Objet inkjet 3D printer utilized a black resin material and a wax/gel-like support material. Solid and pore layers of 150µm and 490µm, respectively, were attempted. After printing, the samples were soaked in a proprietary alkaline solution meant to dissolve out the support material. It was found that the support material did not dissolve out cleanly with the solution, and a combination of water spray and a thin wire were required to remove all the support material from the pores. This resulted in a very low yield of samples, so few usable samples were generated.

The Form2 is a stereolithography (SLA) 3D printer wherein the stage is lowered inverted into a bath of resin. A laser rasters across a defined focal plane, exposing and crosslinking the resin. Then the stage raises one layer height and the process repeats. Once the print is complete, the sample must be soaked in isopropyl alcohol to remove any uncured resin. It was found that for pores capable of being charged below 10kV, the Form2 was not capable of yielding hollow pores. The resin within the pores was partially curing, resulting in partially or fully closed off pores.

Finally, some porous PDMS direct-write 3D printed samples were investigated. These were supplied by a collaborator, Prof. Raney from U. Penn [73]. The samples were roughly

12x12mm square, with tubular pores ~1mm tall, with wall thicknesses of ~0.25mm. Ti/Au electrodes were sputtered onto both sides of the samples in order to achieve a conformal contact with the highly flexible samples. After charging at 7kV, the samples had an effective piezoelectric coefficient of 80pC/N. The PDMS material, however, was relatively hygroscopic, and the charge was found to decay in an hour until no further piezoelectric activity was measured.

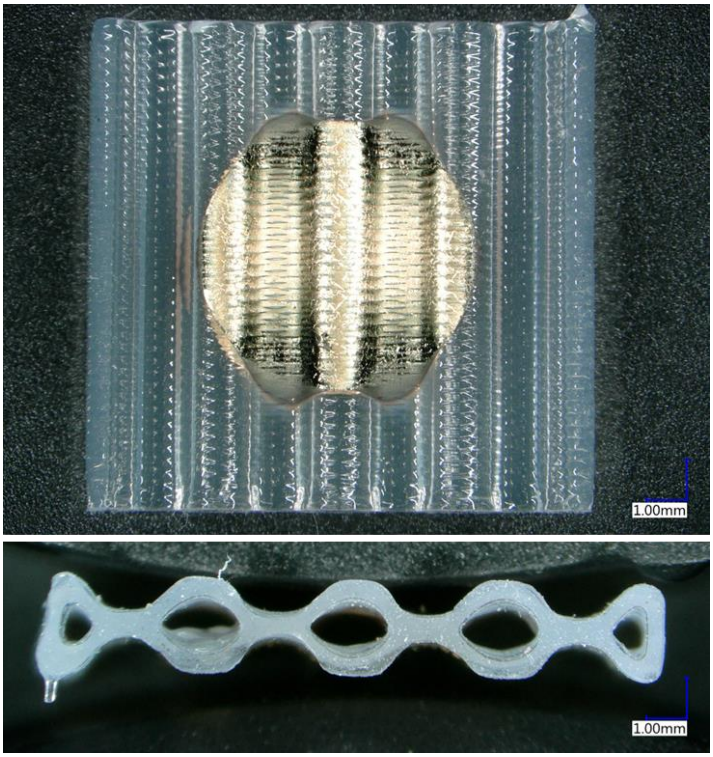

Figure 4 PDMS sample with sputtered electrodes

Direct charging of porous infill electrets

For samples with internal pore structures, direct charging was utilized. While these samples could have been charged using the corona triode, direct charging allowed for additional properties to be measured such as the effective coercive field and remanent polarization. For

these measurements, a Radiant ferroelectric tester was used. This tool applied a bias to the sample through direct contact – either through probe tips or through a high voltage fixture – while measuring the current through the sample. The current flowing through the sample was a combination of polarization current and conduction, requiring subsequent analysis to distinguish.

Samples were taken from the dry box and rinsed briefly with isopropyl alcohol to remove any static or triboelectric charges generated by handling, and adhesive copper foil electrodes were adhered to the top and bottom surfaces. Sample electrodes are required for this test as the probe/fixture electrodes cannot make intimate contact with rough surfaces, and air gaps between the sample and the probe/fixture electrodes could undergo Paschen breakdown and skew the results of the test. The sample was then placed inside the high voltage fixture, and an automated series of tests were run.

The first test was a leakage test, wherein a DC bias is applied and current is measured over time. The bias applied during the leakage test is far below the critical potential for Paschen breakdown, and instead is used to calculate the resistivity of the sample. This test was applied first for each sample as it as well confirmed that the sample was undamaged and was properly electrically connected to the equipment: very high leakage current could mean that the sample was damaged or had absorbed a lot of moisture, and a zero leakage current could mean that the sample was not connected to the equipment properly and an open circuit had occurred.

Nanoscribe

There was a marked difference in the charge stability of the different Nanoscribe samples. The sample with 40µm tall tubular pores demonstrated the highest stability, followed by the sample with simple pillars and 30µm tall pores. For comparison, a single solid 5µm thick sample showed much faster charge decay than either of the other samples.

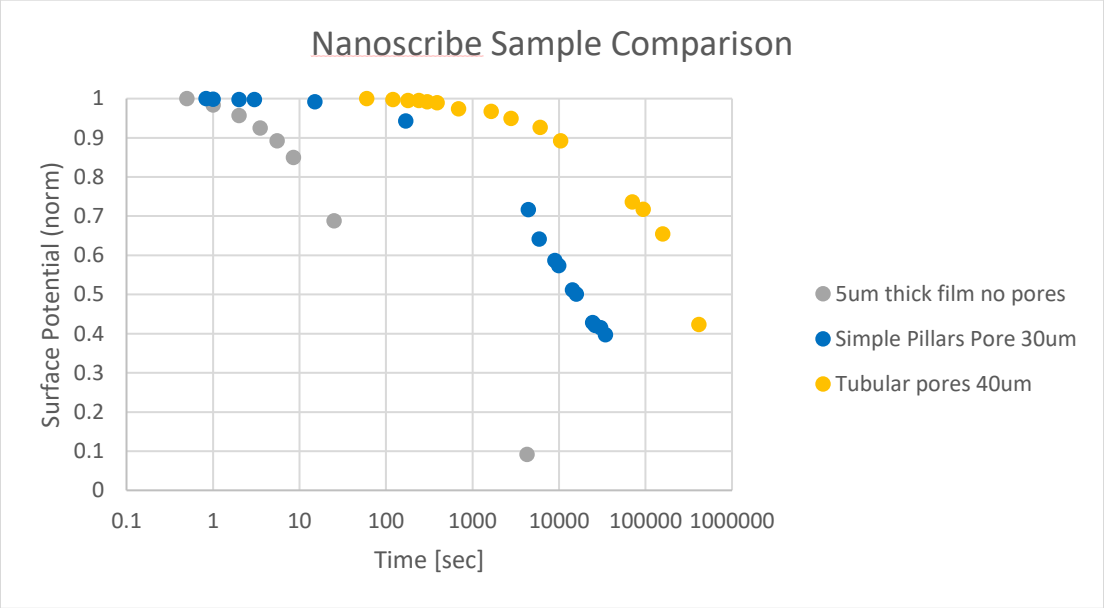

Figure 5 Normalized surface potential comparison between solid and porous Nanoscribe samples

When comparing a 45µm-thick porous sample against a 45µm-thick solid sample, the charge stability started off relatively similar, but on day 24 the porous sample dropped precipitously. On this day, the humidity had increased drastically in the lab. As a result, it appears that with an increased surface area, the porous sample was more sensitive to charge decay due to humidity

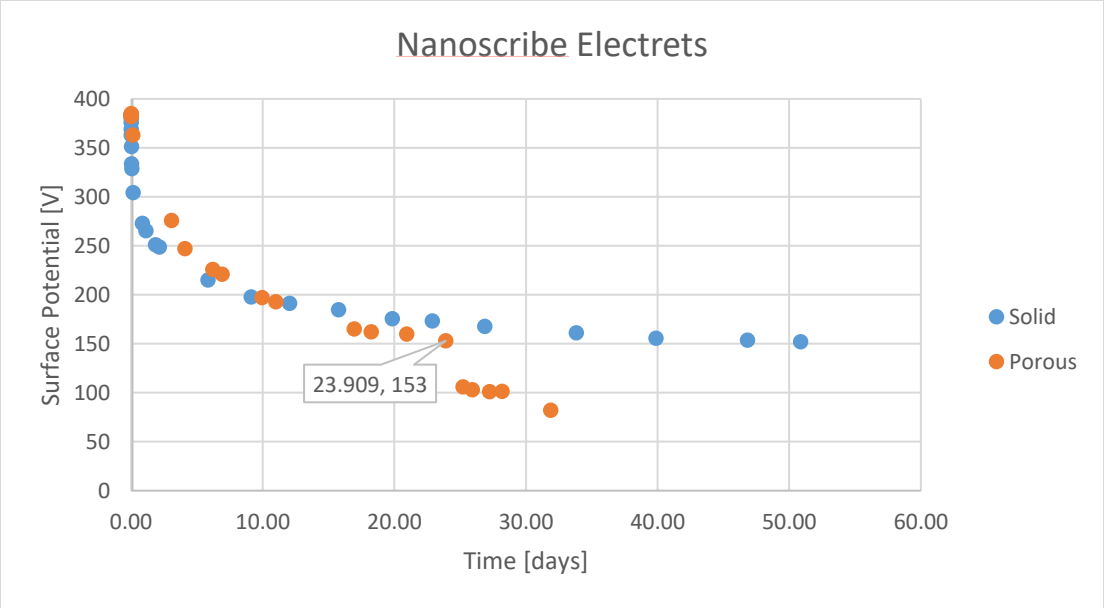

Figure 6 Surface potential ambient decay of solid and porous Nanoscribe samples

Infill Piezoelectrets

Results for the infill piezoelectrets, including figures within this section, were published in 2020 [33]. The infill samples showed a strong hysteresis, switching behavior, and distinct coercive voltages and remanent polarizations. An example nested loop is shown in Figure 7.

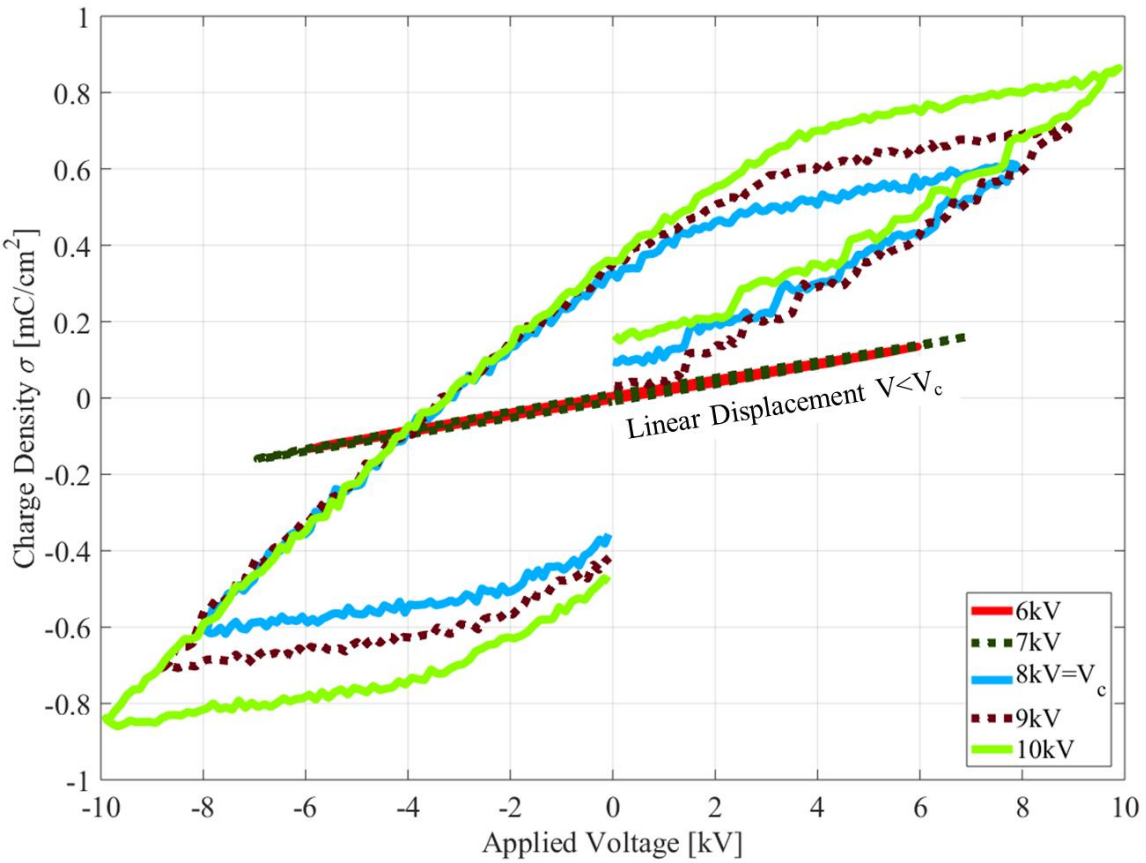

Figure 7 A sample from series "3a" showed a coercive voltage of 8kV and max remanent polarization of ~0.43mC/cm² at 10kV.

The thickness-wise d_{33} piezoelectric coefficient was measured for each sample using a Quasi-Static Piezoelectric Meter from Polyk Tech. Before charging, zero measured piezoelectric coefficient was confirmed for each sample. Immediately following charging, the initial d_{33} was measured. The d_{33} for each sample was subsequently measured multiple times over the course of two weeks, storing the samples in a dry box between measurements. The results from the d_{33} measurements can be seen in Figure 8.

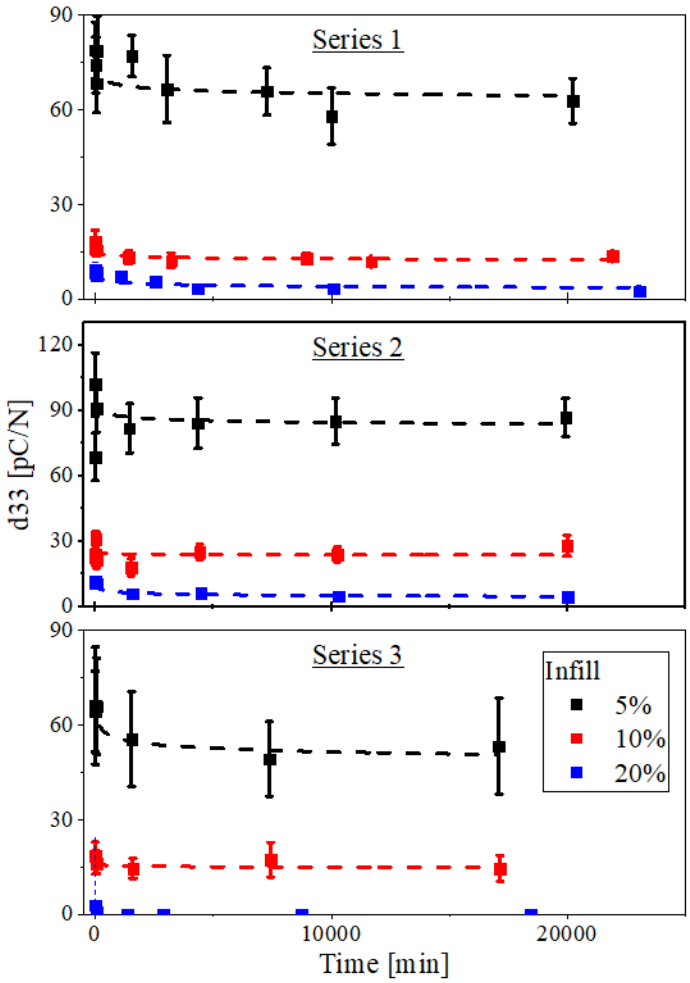

Figure 8 The stability of piezoelectric d33 coefficient was monitored for two weeks after charging. Error bars represent a 95% confidence interval.

The d_{33} was relatively stable for all samples during the two week testing period following an initial drop-off. There was significant variation in d_{33} with infill% in all three series. The highest d_{33} of 262±70 pC/N was recorded for three series 1 samples at 2.5% infill, though these were not plotted as this infill percentage was not capable of yielding viable samples using the other two series' layer thicknesses.

The piezoelectric coefficient was highest for series 2, which used thinner solid layers. As the thinner layers were thought to result in a lower effective Young's modulus, this is in line with the generally-accepted models of piezoelectret behavior.

Future Work

Future work on 3D printed piezoelectrets can utilize newer techniques and equipment to achieve better control over structures, further experimenting with the structure-property relationships in piezoelectrets. There is, for instance, an upgrade to the Nanoscribe that uses a wider field of view lens and larger stage movement envelope that would allow for much larger samples to be produced in less time. This would result in more rapid throughput for experimentation.

Chapter 3: Filament Materials Study

Background

The identified commercial filaments will be purchased and printed using at least one inexpensive (<$4000, Ultimaker 3) and one much higher-resolution but more expensive (>$250,000, nScrypt) FFF 3D printer. The higher resolution of the more expensive printer is likely to allow for better control of the electret properties, though both will be studied to determine the necessity of this cost difference for the properties of interest. The filament materials will be characterized for their crystallinity (DSC) and structure (SEM) both before and after printing to determine the effects of the print parameters on crystallinity and morphology. The moisture uptake of the filaments will as well be characterized by TGA. Samples will be printed using a series of differing extrusion temperatures, print speeds, layer heights, and infill settings. Multiples of each sample and material will be printed to evaluate statistical variance. It is expected for fully amorphous filament materials that the extrusion temperature and print speed will only affect the electret properties via interface formation and not crystallization, and so this factor is not expected to be as important. As-printed solid or "0% infill" samples will be charged via corona triode, and their surface potential measured under both ambient and dry conditions for a period of up to 1 month. Additional samples will be charged and then undergo TSDV measurement.

Motivations and Hypotheses

The goal of this study is to identify the effects that the printing process parameters have on 3D printed electrets, as well as to investigate the effects that commercial additives have on otherwise well-characterized electret polymers.

The materials that will be investigated will be available commercial filaments and 3D printing materials, as well as fabricated composites for direct-write printing. Some filaments can be purchased that are pure polymers that have been shown to be electret materials before, such as PP, ABS, PEI [74], and PLA composites [75]. In those materials, the investigation will focus on the specific effects of 3D printing on the electret properties. In many cases, the commercially-available filaments are not pure materials but contain pigments and other additives [76], such as different color ABS or PLA filaments. The electret performance of those materials will be compared against the pure or "natural" filaments wherever possible.

Besides the materials themselves, the printing process involves a number of parameters which are likely to influence the electret properties. For crystalline or semi-crystalline polymers, the extrusion temperature as well as the cooling rate (fan speed, environment temperature) can result in different degrees of crystallinity [77, 78] which can affect the charge density and charge stability of electrets. The crystallinity of PLA specifically has been shown to be highest with an extrusion temperature of 210ºC [76], so a range of extrusion temperatures around this value will be investigated to determine if crystallinity affects electret charge.

Materials and Methods

Filament Materials Chosen

- PLA (Ultimaker) in white, green, black
- PLA (Protopasta) in white
- Ryno
- HIPS (Ultimaker)
- Bendlay
- Layfomm40 and 60
- PLA (Ultimaker) "natural" unpigmented, for comparative study of extrusion temperature effects on crystallinity and charge stability

Sample Preparation

For filament material properties characterization, circular coupons of 45mm diameter and 1mm thickness were printed at 100% infill. These samples were printed on an Ultimaker 2 3D printer. Solid infill was chosen to minimize the potential influence of pores which could undergo Paschen breakdown. The purpose of these coupons was to compare the relative dielectric and electret properties of various commercially-available filament materials.

Coupons were printed in batches of 9, as this was the maximum number that could fit on the print bed at a time. Once printed, the coupons were removed and placed in ziplock bags in a nitrogen dry box to minimize water absorption. Each filament material was loaded and extruded until the previous filament material was pushed out of the extruder. The filament was allowed to extrude for the entire duration of the Ultimaker "filament load" cycle,

approximately 1 min. Then a single coupon was printed and discarded to ensure that there was minimal chance of cross-contamination between materials. Then, at least 20 samples were printed for that filament material before moving onto the next, so that all coupons of a given filament material were printed as close together in time as possible while minimizing cross-contamination likelihood. Samples were kept in the nitrogen dry box after printing and between surface potential tests.

Corona Triode Charging

For non-contact charging of electret samples, a corona triode was utilized. The triode was constructed of three parts: a discharge needle, a grid, and a ground plate on which the sample was placed.

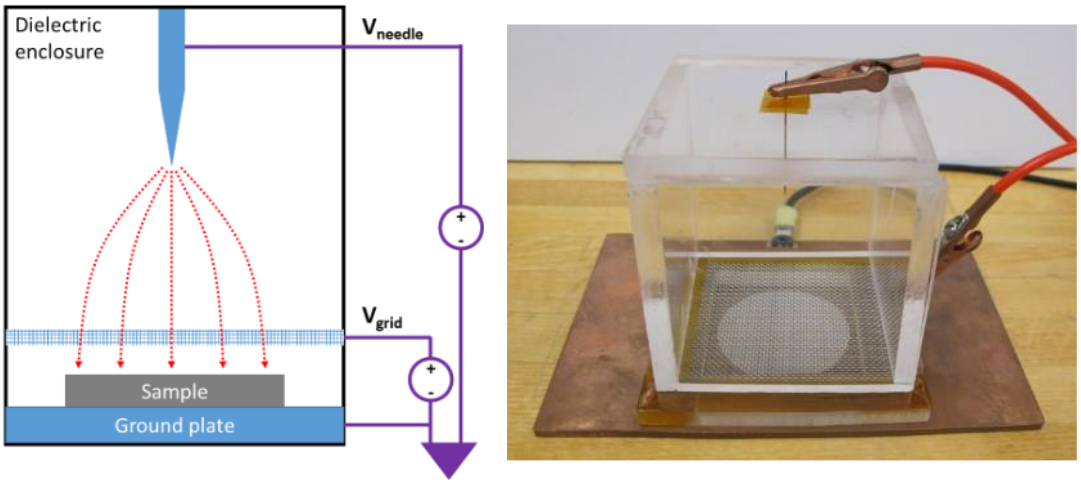

Figure 9 Corona triode circuit (left) and fixture (right) used for charging 3D printed coupons.

A tungsten DC probe tip was used as the discharge needle, and the grid was stainless steel, with the body of the fixture made of acrylic. When the needle is brought to a high voltage, charge species are generated due to the high curvature of the needle tip. The potential difference between the needle and grid accelerate the charge species towards the grid and further towards the ground plate, onto the sample. The grid is held at an intermediate potential from the needle

and ground, and acts to screen the charge species for polarity and to establish the bias potential of the charges as they reach the sample. As an example, for a needle potential of +5kV and a grid potential of +500V, the sample immediately following corona charging will be approximately +500V. The sample is kept under corona discharge for 10mins, as this was found to allow sufficient time for the sample surface to come up to the full potential of the grid.

Before each sample was charged, it was removed from the dry box and rinsed briefly with isopropyl alcohol to remove any static or triboelectric charges generated by handling. The sample was then dried using compressed nitrogen and allowed to finish air drying for a few minutes before being placed on the ground plate. Zero initial potential was then confirmed by measuring with the surface potentiometer before the triode assembly was placed above the sample and the corona charging was started. Immediately following the charging procedure, all conductive surfaces within the enclosure were grounded and the triode assembly was removed. The sample was then measured with the surface potentiometer for the first 45min before being removed from the ground plate and placed into the dry box. This was done to minimize sample exposure to ambient moisture while still providing sufficient time for another sample to be charged before the next surface potential monitoring time step from the previous sample.

Thermally-stimulated potential discharge (TSPD)

For the set of natural PLA samples printed at different extrusion temperatures, thermally stimulated potential decay (TSPD) measurements were made using the same probe as the corona charging/ambient temperature decay experiments. For charging, the same procedure was utilized as in the previous section. Immediately following corona charging, the sample was moved to a

hotplate and the surface potential probe was centered over the sample. A Labview script was used to control the temperature of the hotplate at a linear heating rate while logging the surface potential measured by the surface probe. The hotplate was cooled down to room temperature before each test.

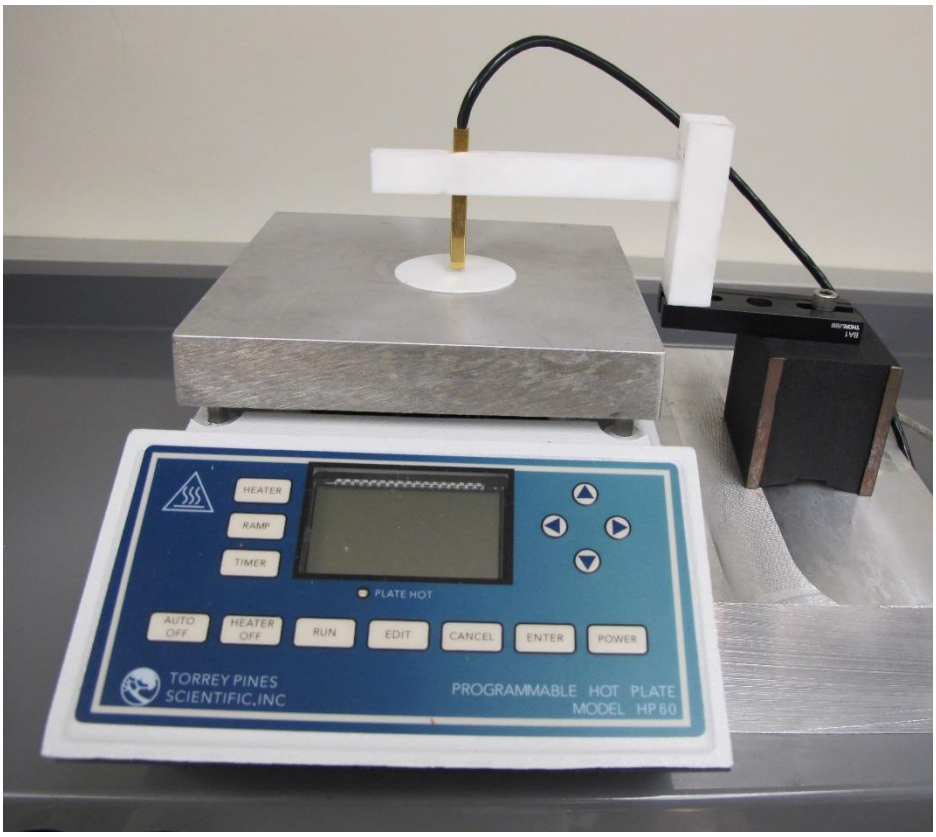

Figure 10 Hotplate and voltmeter probe configuration for TSPD measurements

Results and Discussion

Dielectric Spectroscopy

The dielectric spectra for many of the filament materials show a strong temperature effect, as illustrated by the spectra for white PLA in Figure 17. The initial spectra from 25-45ºC show no relaxation peaks. Starting at 50ºC, a relaxation peak can be seen emerging from the low

frequency (left) side of the plots, which is in line with the glass transition temperature for PLA of 60ºC .

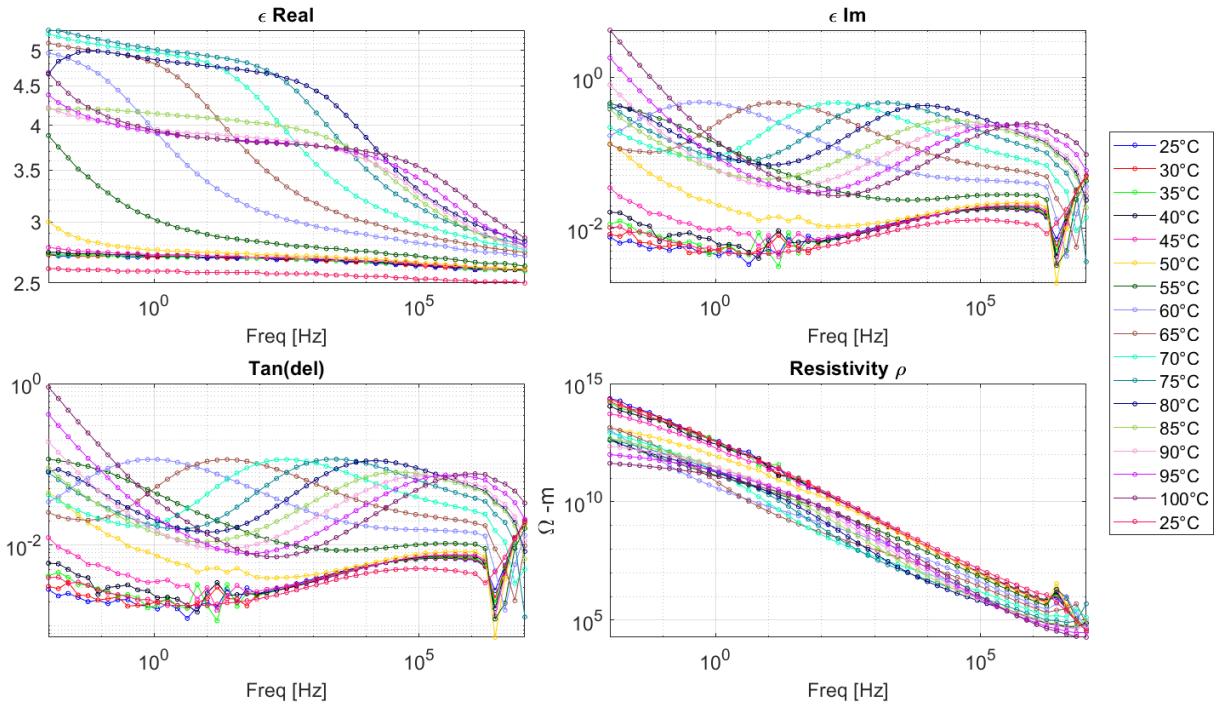

Figure 11 The spectroscopy results for white PLA from Ultimaker, with relaxations emerging starting at 50ºC (yellow line).

The black PLA (Ultimaker) had two relaxation peaks with the first present at room temperature, indicating that the pigment used either has its own dielectric relaxation at a higher energy than the bulk PLA, or that it is modifying the PLA chemically. As well, the black PLA had a slightly lower resistivity than the white PLA across all temperatures. The green PLA also showed a similar two-peak spectrum to the black.

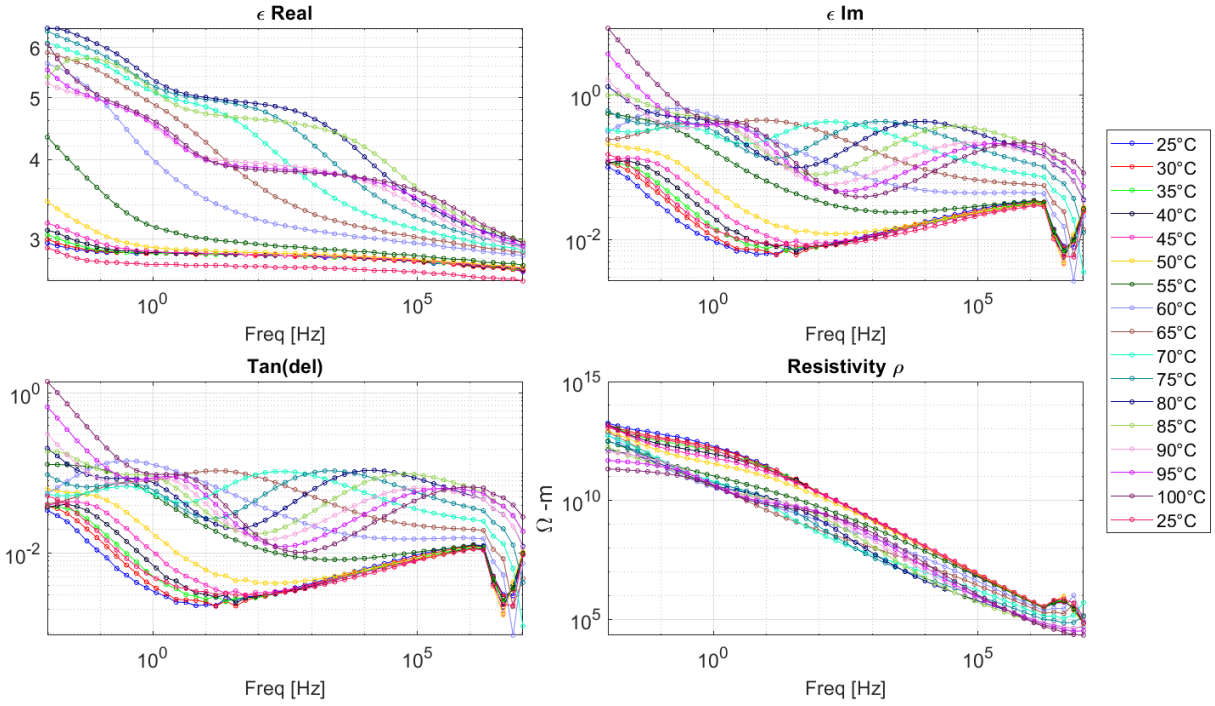

Figure 12 The spectroscopy results for black PLA (Ultimaker) show relaxations in ε" starting at room temperature.

The ε" curves could then be fitted with the Havriliak-Negami equation using the WinFIT program from Novocontrol to extract the associated time constants of the relaxation processes, and a resultant Arrhenius plot as shown in Figure 13. This Arrhenius plot matches well with the observed behaviors in [79] for the glass transition of PLA. The secondary processes observed in that study at much larger time constants, associated with stabilized dipoles, were not observed in these samples as the dielectric spectroscopy samples were not charged beforehand.

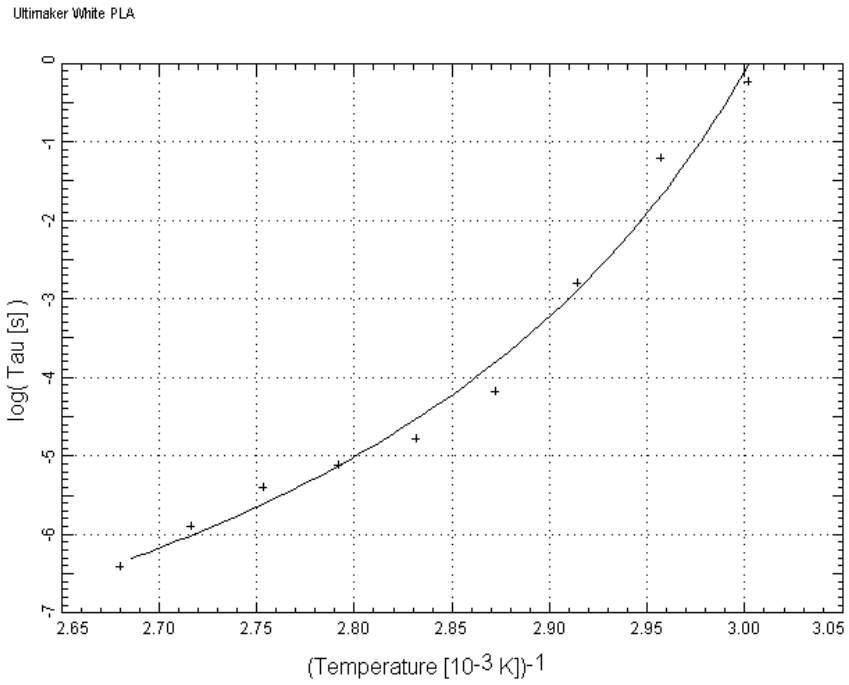

Figure 13 The extracted time constants are plotted in an Arrhenius plot for the white PLA from Ultimaker.

The extracted dielectric constants, loss tan(delta), and resistivities for the studied filament materials are depicted in Table 3. The large number of previously-unknown values for these filaments' properties can provide additional insight for other researchers studying 3D printing for dielectric structures or substrates for other electronics.

Table 3 Table of measured dielectric properties. Green are values measured in this study that were not previously measured or reported for these filaments.

Color/Type	Material	Polymer(s)	Source	er'	tan(d)	resistivity
unspec.	ABS	ABS	Ultimaker	2.69	0.012	
white	TPU95a	TPU	Ultimaker	4.12 [1MHz]	0.058 [1MHz]	vol 10e11 [Ohm*m] surf 2e14 [Ohm]
White	PLA	PLA	Ultimaker	2.7 [1MHz] 2.72 [-2hz] 2.6 [1MHz]	0.008 [1MHz] 0.0028 [-2hz] 0.00656 [1MHz]	2.34e+16 [-2hz]
Black	PLA	PLA	Ultimaker	2.96 2.72	0.0343 0.0128	1.77E+15
Green	PLA	PLA	Ultimaker	2.92 2.62	0.0055 0.0145	1.12E+15
White	PLA	PLA	Protopasta	2.53 2.5	0.00253 0.00571	2.70E+16
clear	Ryno	copolyester/PET	Matterhackers	3.07	0.00101	5.78E+16
nat	HIPS	HIPS	Matterhackers	2.8	<0.003	>2E+15
clear	Bendlay	ASA	Matterhackers	2.29	0.0567	1.39E+15
nat	PP	PP	Ultimaker	1.91 [1MHz]	0.003 [1MHz]	>10e16

Surface potential decay over time

The normalized results of all ambient temperature surface potential decay tests are shown in Figure 22. Comparing the four PLA filaments against one another, the black PLA demonstrated the lowest charge stability, losing 30-35% of its initial charge within the first 28 hours (~100,000 sec). From the dielectric spectroscopy results, the black PLA had lower resistivity as well as a measured relaxation peak starting to emerge at room temperature. Interestingly, the green PLA had these same behaviors in the dielectric spectra, but its charge decay response is more in line with the two white PLA filament materials. Without knowing the specific chemical makeup of the pigments used, more experiments would have to be run to determine why the green and black PLA filaments differed so greatly in charge stability while showing similar dielectric responses.

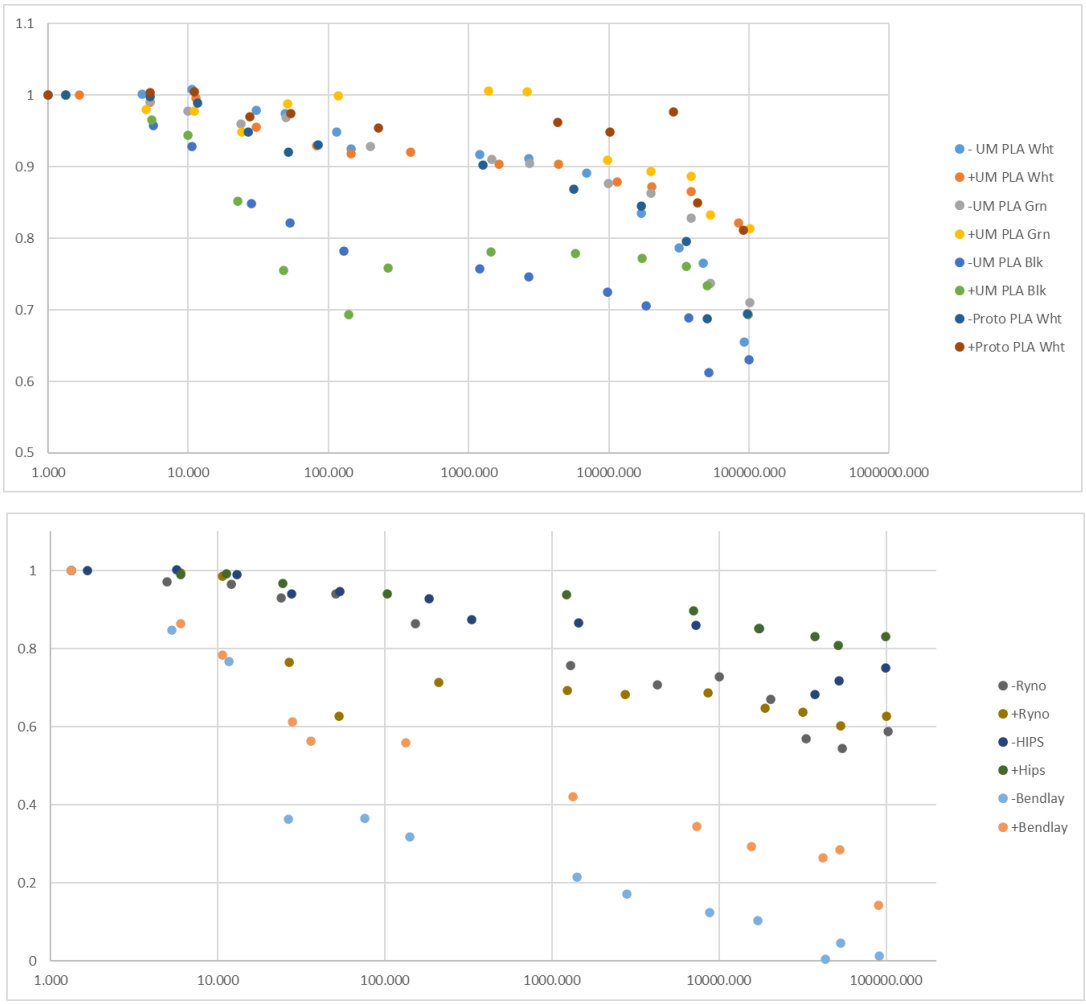

Figure 14 Normalized surface potential decay at ambient temperature, dry box conditions, for all studied filament materials. Separated into two plots for clarity.

The two Layfomm filaments were printed and tested similar to the other filaments, but all surface potential on all samples decayed within a day, and so were not included in the comparison charts in Figure 22. Bendlay exhibited the lowest 2-month charge stability.

Thermally Stimulated Potential Decay

The voltage over temperature data from the TSPD measurement was measured using the noncontact surface probe, resulting in a decay curve such as one below:

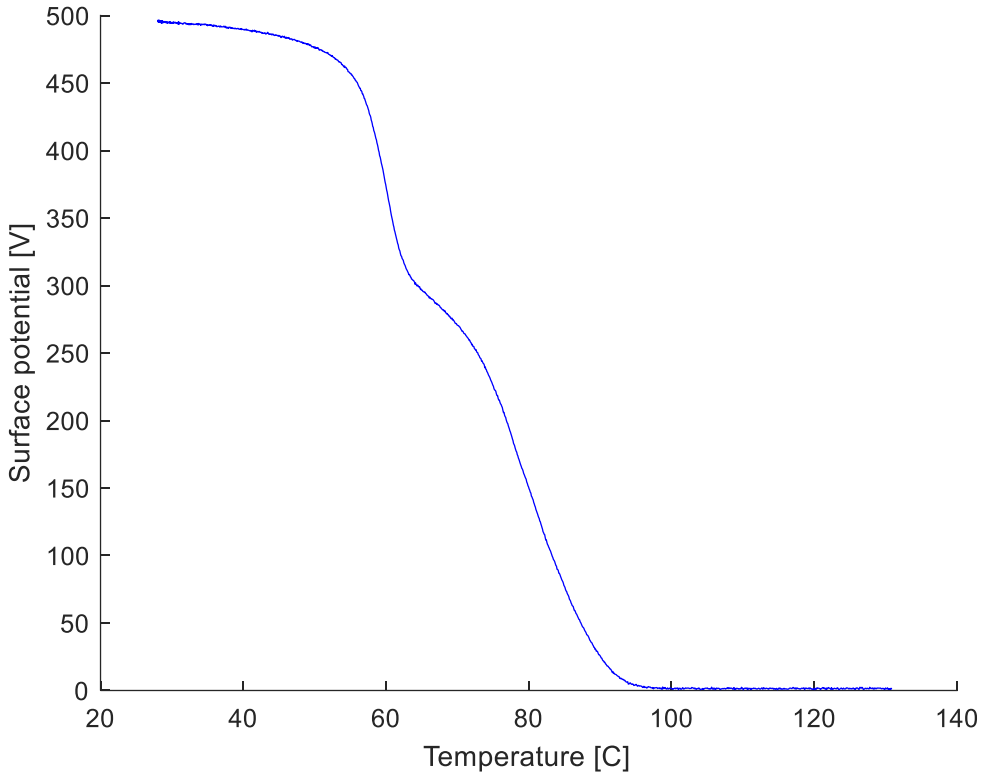

Figure 15 As-measured thermally-stimulated potential decay for natural PLA printed with 230ºC extrusion temperature

Next, the current was calculated by differentiating the voltage and dividing by the capacitance of the sample, resulting in a current verses temperature plot as shown below:

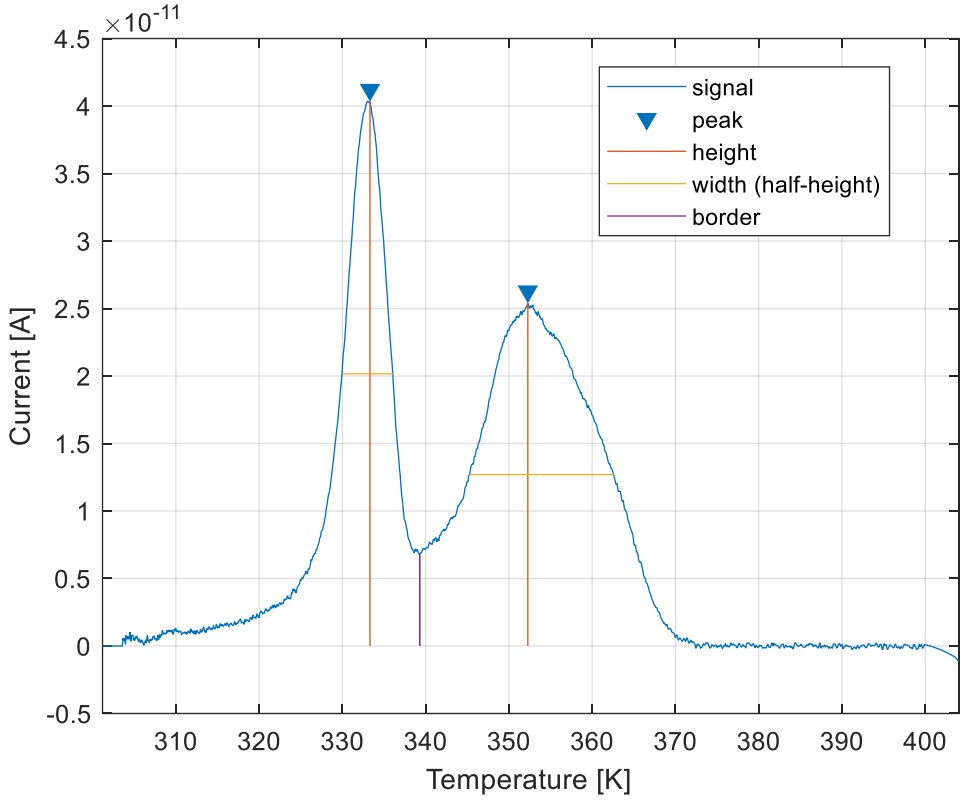

Figure 16 Calculated thermal decay current for natural PLA printed with 230ºC extrusion temperature. Peaks were located using "peakfind" function in Matlab

When looking at the TSPD results for the natural PLA study, there are two peaks to consider. The lower temperature peak, ranging 55-60ºC, and the higher temperature peak, ranging 77-85ºC. The high temperature peaks, however, have a lower error and a more clear trend. The samples extruded at 210ºC showed the highest second peak temperature, significantly higher than the 200ºC extruded samples, with a decreasing trend in peak temperature at 220ºC and 230ºC.

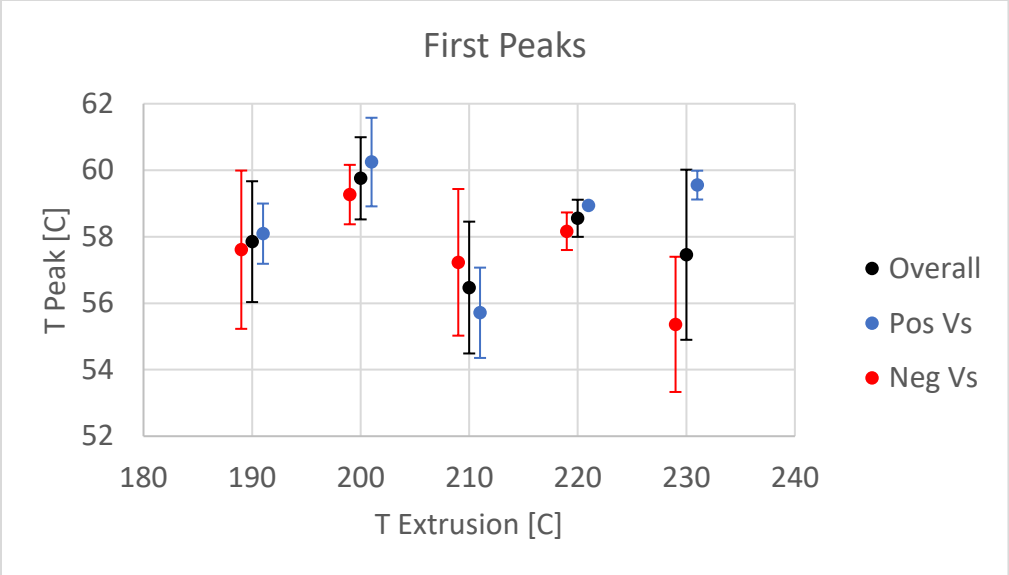

Figure 17 Low temperature/first decay peak temperatures for all natural PLA samples

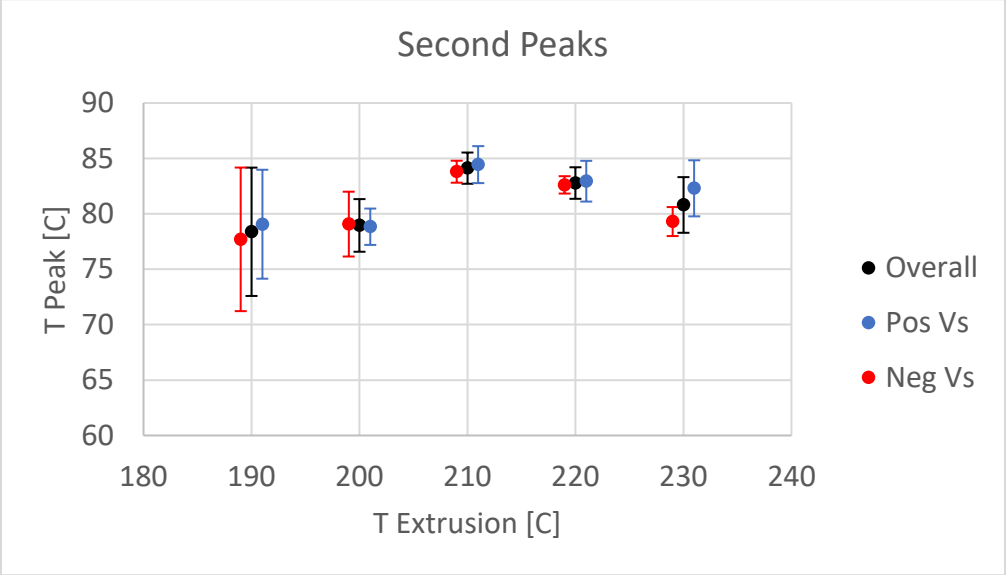

Figure 18 Higher temperature/second decay peak temperatures for all natural PLA samples

The activation energy can be calculated from the peak temperature by using reaction kinetic theory as shown in [48]. The attempt-to-escape frequency ν is fixed at an estimated value of $1x10^{13}$, and by using the equation below the activation energy is calculated, where β is the heating rate. Errors for these estimates were approximated to be within ~0.1 eV so long as the unknown "true" value of ν was within two orders of magnitude.

$$E_a = k_b * T_{peak} * (\ln\left(\mathrm{v} * \frac{\mathrm{T}_{peak}}{\beta}\right) - 3.47)$$

The activation energies for the two observed peaks across all natural PLA samples were 0.9806±0.0049 eV and 1.0526±0.0058 eV, respectively. These values fell within the range of activation energies found in literature for PLA associated with the glass transition molecular motion [75, 80] for samples charged at room temperature (77 kJ/mol, equivalent 0.7980 eV) or after heating to 90ºC (222 kJ/mol, or 2.3009 eV).

Crystallinity

Crystallinity was determined using DSC analysis. Filament measurements were taken using two heat cycles to simulate thermal cycling due to extrusion. The first cycle for each sample was up to the "extrusion" temperature, with the second heat cycle used to determine the crystallinity of the filament due to this first "extrusion" heat cycle.

For measurements on printed samples, five portions were cut from 3D printed coupons and averaged for each extrusion temperature. While there was some variation in crystallinity across extrusion temperatures, the absolute differences across all samples was within 1.5%.

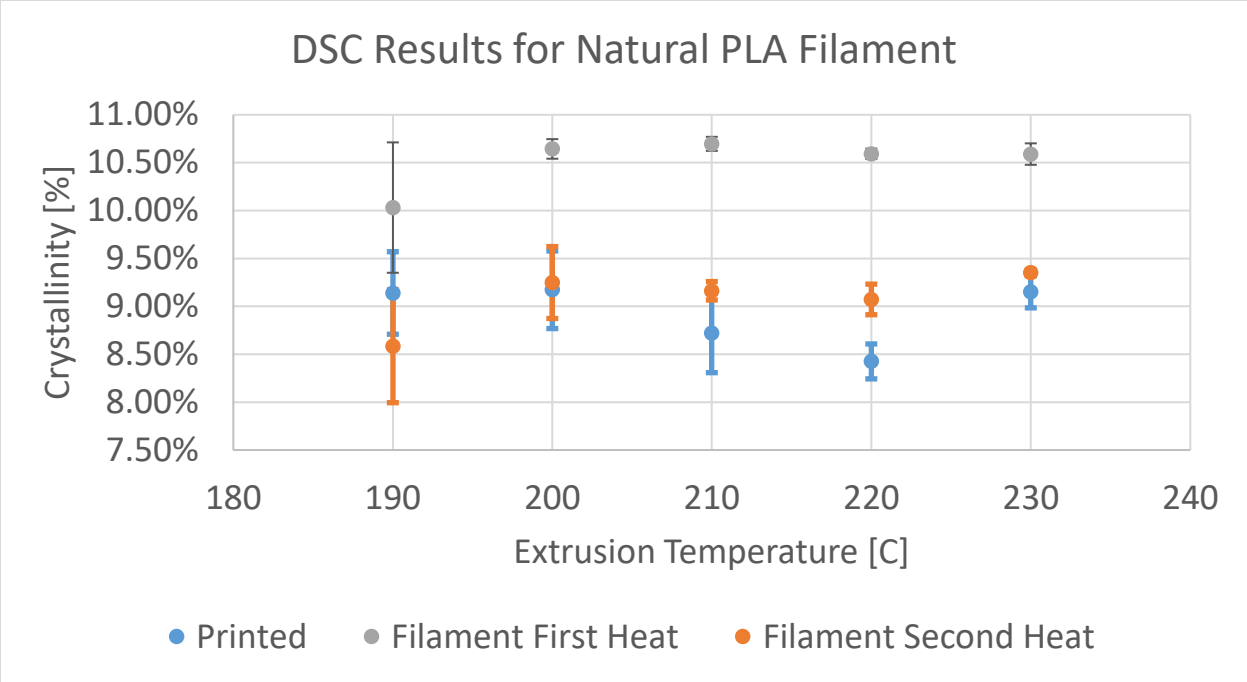

Figure 19 Crystallinity vs extrusion temperature, printed coupons compared with filament samples. Error bars mark one standard deviation (plus and minus) for each data point.

Since the crystallinity values fell within a relatively narrow range, it is not clear whether crystallinity alone can account for the differences in TSPD peak temperatures, or if there are other secondary effects from extrusion temperature such as inter-layer bonding or layer remelting.

Future Work

Future work could be directed at looking at the optimization of thermal history of samples, both during and before 3D printing. Filaments such as polypropylene could show more change in crystallinity with extrusion temperature. It has also been known within the electret community that charging electrets at elevated temperatures or annealing after charging can affect their charge density or stability [81, 82]. A study of different platform or enclosure temperatures,

or of post-print annealing, may elucidate further charge density or stability optimizations by employing the comparison of charged and un-charged samples using dielectric spectroscopy.

Chapter 4: Delignified Wood

Background

Prof. Hu's group has long been investigating wood and other cellulose materials. By utilizing techniques from the paper making process, they removed lignin from wood to achieve a porous pure-cellulose material that has been investigated directly and in composites for a variety of applications [83, 84]. One such interesting material is wood that has had the lignin removed without going through a pulping process beforehand, resulting in a pure cellulose porous structure. This delignified wood has an open, continuous pore structure with pore sizes at a reasonable size for Paschen charging (10-100 μm). The pores are also a similar size and overall layout to existing engineered piezoelectrets. An SEM cross-section of a delignified basswood sample is shown in **Error! Reference source not found.**.

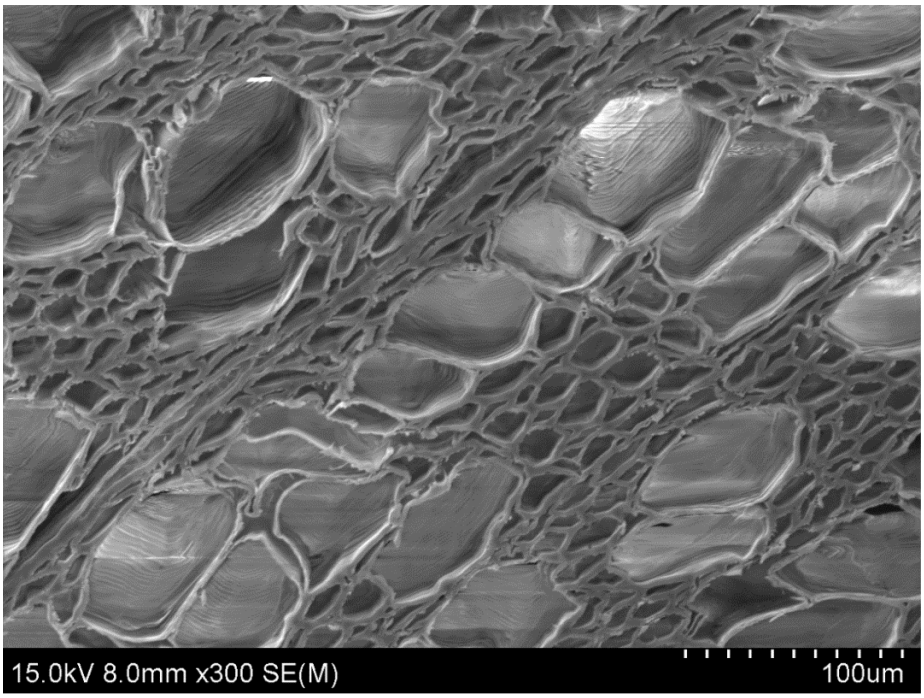

Figure 20 SEM cross-section of delignified basswood. Some distortion of the pore structure has resulted from cutting the sample with a razor blade.

Motivation and Hypotheses

While the natural structure of delignified wood would indicate a likely porous electret candidate, cellulose itself will not be expected to match the dielectric properties of more optimized electret materials such as fluoropolymers. The work in this chapter represents the initial investigation into the properties, capabilities, and limitations of delignified wood as an electret.

Sample Characterization

Sample Preparation

Delignified basswood ~1mm thick were prepared by Chao Jia in Prof. Hu's lab at UMD. The delignified wood was then cut into 2x2cm square samples using a razor blade. Gold electrodes with a titanium adhesion layer were sputtered onto each side so that intimate electrical

contact could be made with the rough delignified wood surface. A shadow mask with a 1x1cm opening was employed to provide repeatable electrode sizes, and care was taken to align the front and back electrodes, as shown below.

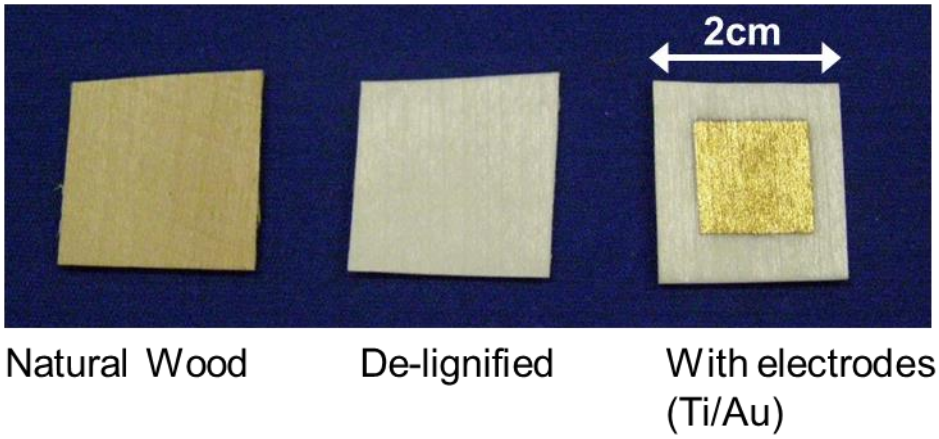

Figure 21 Wood samples cut to size, and sputtered with Ti/Au electrodes for electrical characterization

Samples were stored in a desiccant-filled dry box after sputtering until characterization to minimize moisture uptake. In addition to SEM cross-section, a delignified wood sample was imaged using an x-ray CT scanner, which confirmed the pore sizes and relative distribution from the SEM image. The calculated Paschen breakdown fields are shown inset in the figure below.

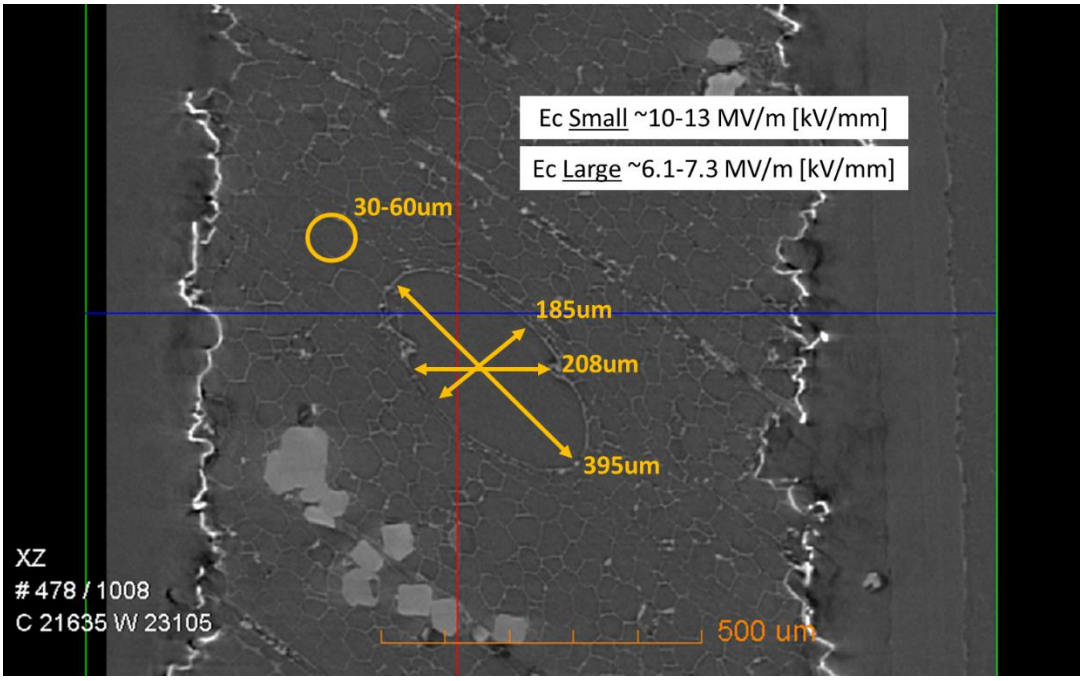

Figure 22 CT cross sectional image of delignified wood with measured pore sizes. Calculated Paschen breakdown fields are inset. Bright edges are due to sputtered electrodes.

Direct Charging

Dried samples were characterized for charge hysteresis using a Sawyer-Tower circuit [85]. It consisted of a waveform generator (V_{in}) which fed through a Trek 10/40a high voltage amplifier to apply a single up/down triangle waveform to the sample. An op-amp and measure capacitor (C_m) then amplifies the low current signal from the charging sample (C_s), as shown below. This circuit allowed the use of standard low-voltage equipment like a benchtop oscilloscope to read the current through the sample without being exposed to the high voltages used to charge the sample.

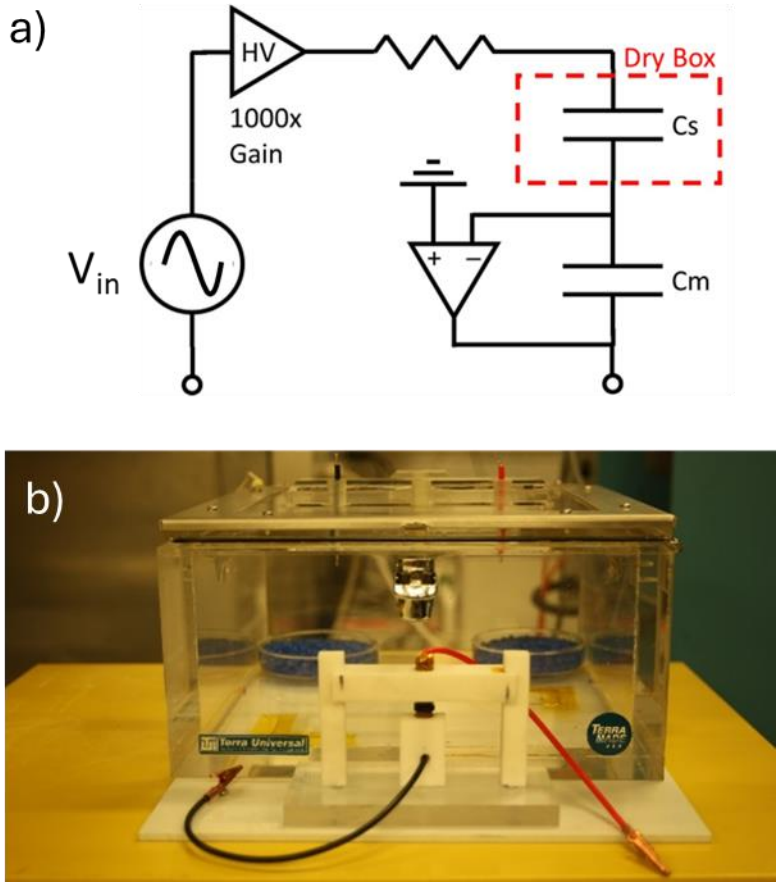

Figure 23 Sawyer-Tower circuit (a), and charging dry box (b) used for delignified wood charging characterization

De-lignified wood demonstrated characteristic ferroelectret behavior, namely linear sub-critical voltage behavior, large change in charge at/above a critical voltage, and a remnant charge at zero applied voltage, and roughly symmetrical switching behavior at negative applied voltage. The critical voltage was found to agree with the calculated Paschen breakdown voltage for the largest cellulose pores. Sample breakdown occurred at higher voltages (above 10kV), meaning that direct charging would not likely be able to address the smaller pores. By comparison, the natural wood sample demonstrated no switching behavior, instead only showing a "football" shaped curve indicative of a lossy or low-resistivity capacitor.

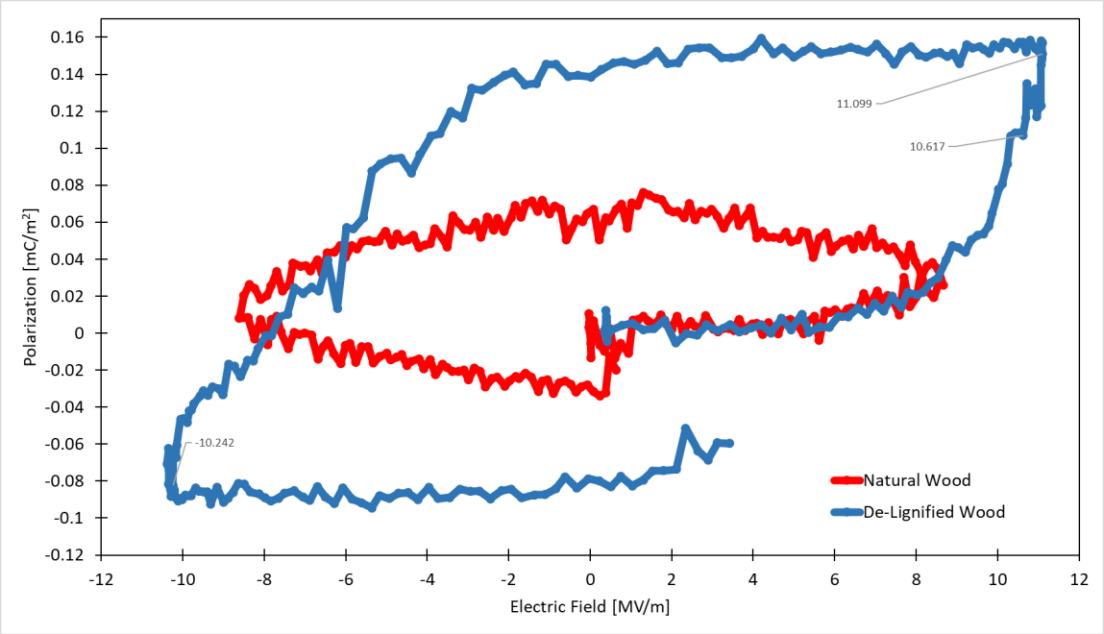

Figure 24 Direct charging hysteresis comparison of natural and delignified basswood samples, showing the lack of remanent polarization in the natural wood sample.

Moisture Absorption

The delignified wood was predicted to be hygroscopic, as natural wood does absorb moisture from the environment using the Hailwood-Horrobin relation; typically as much as 10% or more at typical ambient conditions [86]. Samples were taken from dry box storage and allowed to sit at ambient for different amounts of time. These samples were characterized through thermo-gravimetric analysis (TGA) – staying below temperatures where cellulose degradation would begin – and plotted over time below normalized against a fully hydrated sample that had been at ambient humidity for over a day.

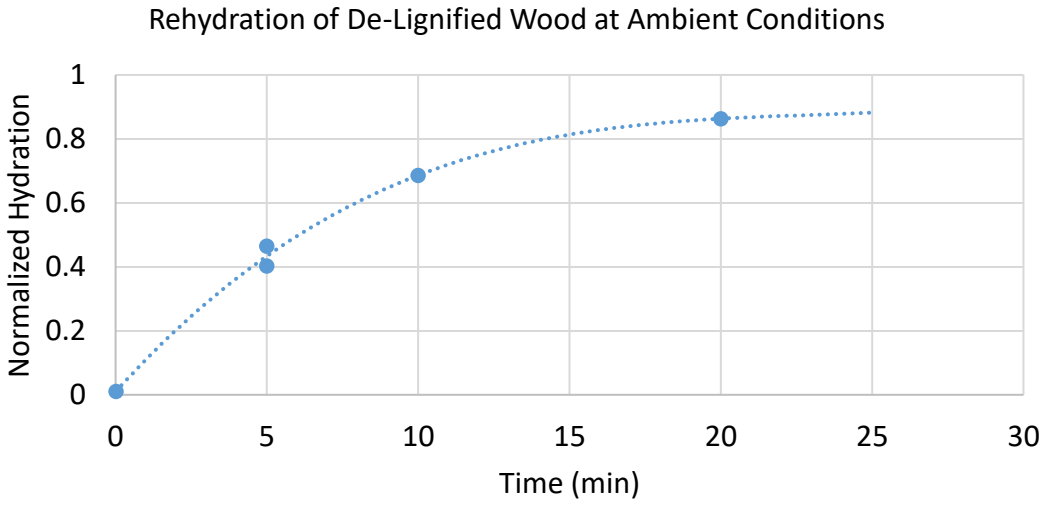

Figure 25 Normalized hydration of white wood exposed to ambient humidity for up to 20 minutes

Re-hydration (moisture content measured normalized against equilibrium moisture content) of these samples was found to occur within 20 minutes at ambient moisture in the Spring season.

Dielectric Spectroscopy

Four different samples were characterized using dielectric spectroscopy to determine the relative dielectric behaviors of delignified, natural, and packaged delignified wood. For each sample, the real ε' and imaginary ε" components of relative dielectric constant, loss tangent

tan(del), and resistivity ρ were plotted using Matlab.

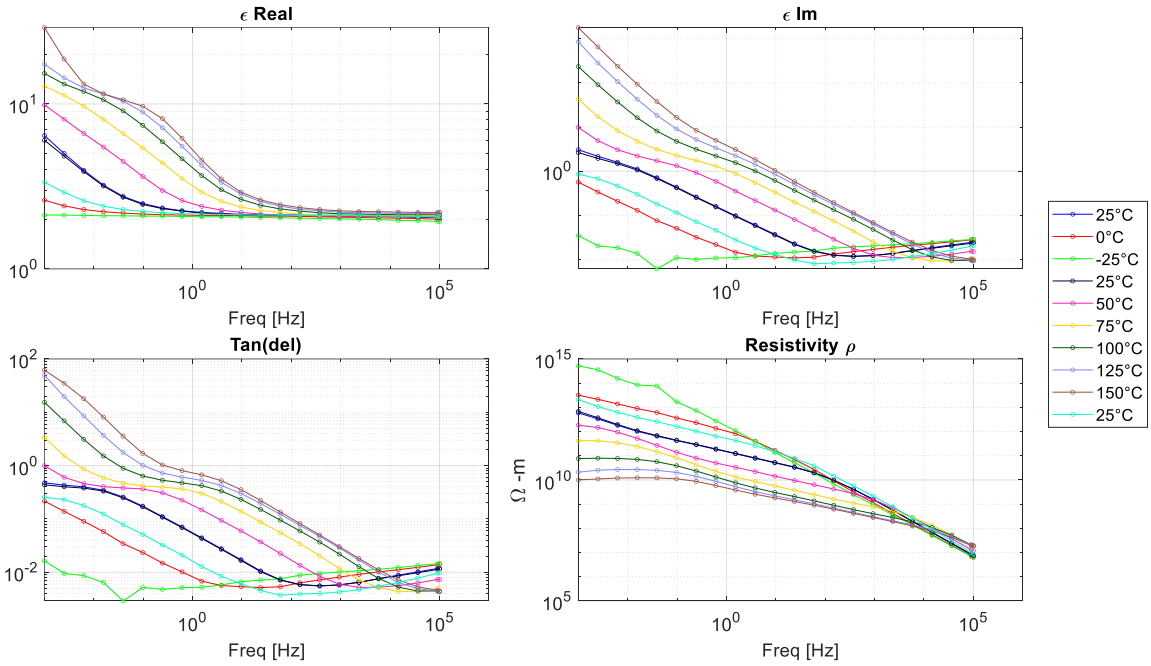

Figure 26 Natural wood dielectric spectroscopy results.

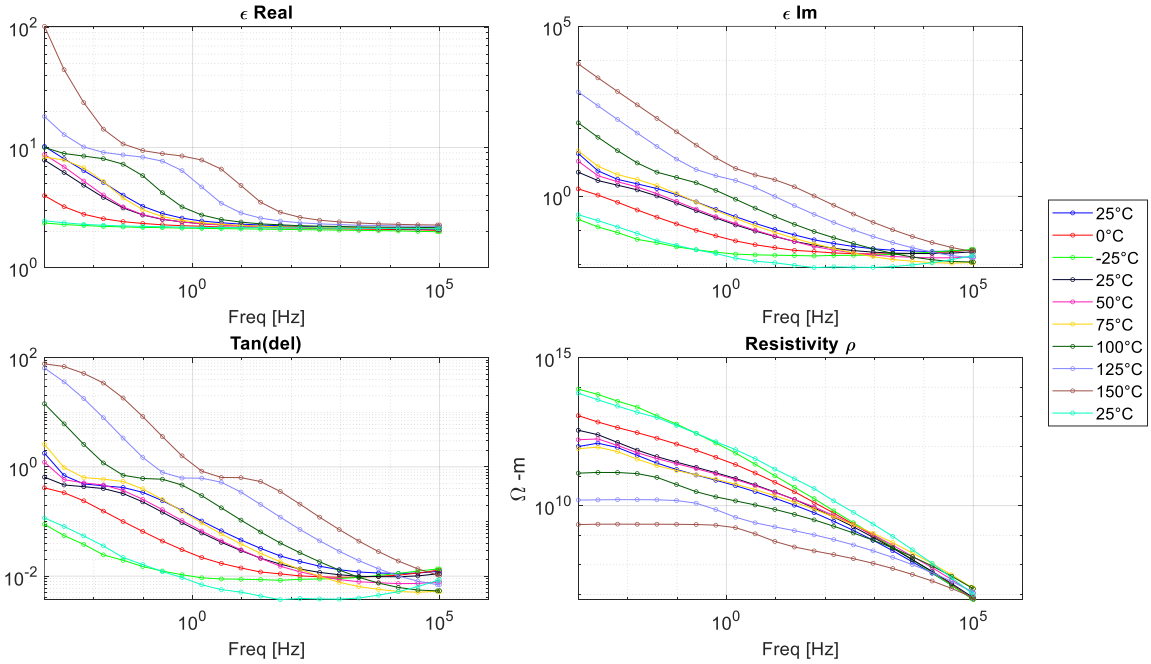

Figure 27 Delignified wood dielectric spectroscopy results.

Results and Discussion

When comparing the natural and delignified wood dielectric spectroscopy data, the overall trends are very similar. A series of relaxation peaks can be seen emerging from the low frequency regime starting above -25ºC. These could be attributed to absorbed moisture, or possibly electrode polarization [87]. A strong simultaneous increase in ε' and ε" is also evidence of these behaviors. An interesting distinction between these two samples is in the conductivity behavior. The delignified wood shows a significant decrease in resistivity at higher temperatures. This could possibly be due to increased mobility of absorbed water, or from partial carbonization. The second possibility is further reinforced by the fact that delignified wood samples would change color from pure white to yellow/tan after heating much above 100ºC.

Two additional delignified wood samples were enclosed in a polypropylene vacuum-seal bag: one with the bag unsealed, and one vacuum sealed. These samples were only tested at room temperature to avoid further heat deforming the bag and affecting the results.

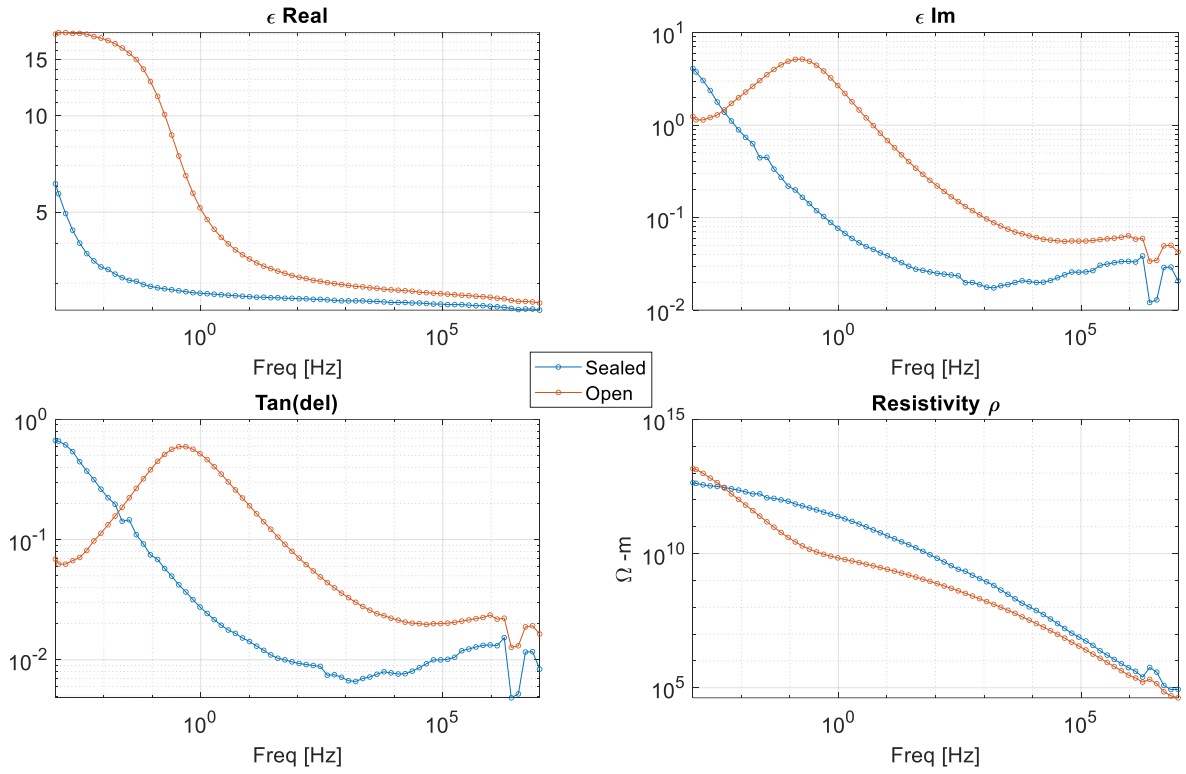

Figure 28 Delignified wood in polypropylene bag, sealed and unsealed for comparison, at room temperature.

These results show a very distinct difference, with a strong relaxation peak present in the unsealed sample. The dielectric spectroscopy and TGA analyses both confirm that the delignified wood has a very high hygroscopic tendency, and the absorbed water has the effect of providing dielectric relaxation. This corresponds with the results from charging, where samples charged in a dry environment demonstrated a remanent polarization, while samples in ambient environment (especially during more humid times of year) are far more conductive and the observed charging behavior is no longer seen.

Future Work

Delignified wood has been shown to be an interesting dielectric material whose naturally-structured pores can be charged via Paschen breakdown. The largest limitation is its hygroscopic

nature, so one aspect of future work could be to investigate composites using delignified wood and more moisture-resistant materials, or other modifications to cellulose that make it more hydrophobic [88, 89]. It would also be interesting to investigate other species of wood with different pore structures, given that the delignified basswood samples in this study were only able to generate charge with the smaller portion of large diameter pores, leaving much of the internal pore structures under-utilized. Composites using polymers could help with breakdown strength but counteract some of the benefits of delignified wood as a renewable material.

Chapter 5: Discussion and Conclusions

Review of Findings

3D printed porous electrets

The infill porous electrets demonstrated clear charging hysteresis during their direct charging cycles. Below the critical voltage, a linear dielectric behavior was seen. At/above the critical voltage, a remanent polarization was observed, increasing with increasing applied voltage. The observed critical voltage as well agrees with the Paschen curve for each sample's given pore size. There was a large difference in measured effective piezoelectric constant between samples of different infill %. This behavior was reasonably explained by considering the infill pores as clamped charged membranes deforming under load, though further work would need to be done with different infill shapes to validate this model, or to use numerical models like finite element analysis.

Dielectric Spectroscopy

The complex dielectric behavior was measured for 10 different commercially-available 3D printing filament materials, noting distinctions between PLA filaments of different colors and the presence or absence of relaxation peaks at elevated temperatures.

Surface potential decay

The relative charge density of these polymers was measured for a two month period. Significantly faster charge decay was noted for black PLA from the three other PLA filaments studied.

PLA print temperature study

An additional study was conducted on unpigmented PLA across five different extrusion temps within the manufacturer's recommended extrusion temperature range. The extrusion temperature was shown to affect the electret behavior, as determined by thermally stimulated potential decay. There was not a clear direct trend of charge stability that correlated with crystallinity, so further study would be required to determine possible secondary effects from extrusion temperature (such as inter-layer adhesion, previous layer remelting, etc) that could explain this measured behavior. From [76], their 210ºC PLA samples showed the highest degree of crystallinity, though this specific result was not replicated in this study.

Summary of Contributions

- Demonstrate first fully printed FFF piezoelectret – publication
- Investigate alternative 3D printing methods for electrets
- Characterize performance of 3D printing filaments for electrets
- Investigated delignified wood as electret material

Appendices

Appendix A: Dielectric Spectroscopy of 3D printing filaments

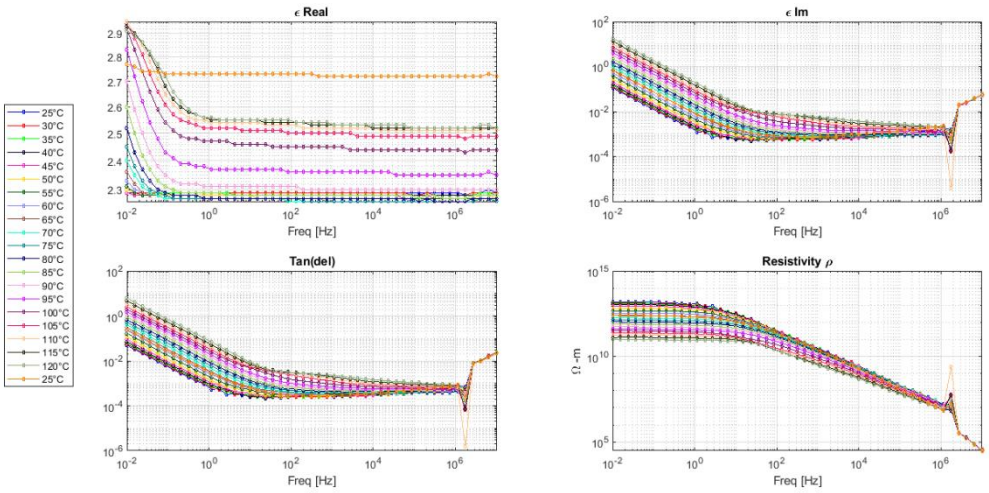

App.A 1 Bendlay clear

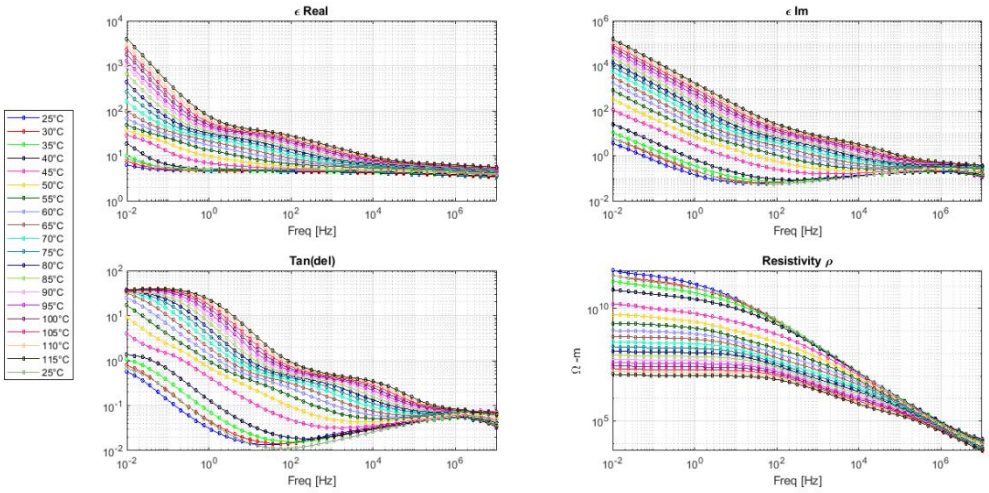

App.A 2 Layfomm40

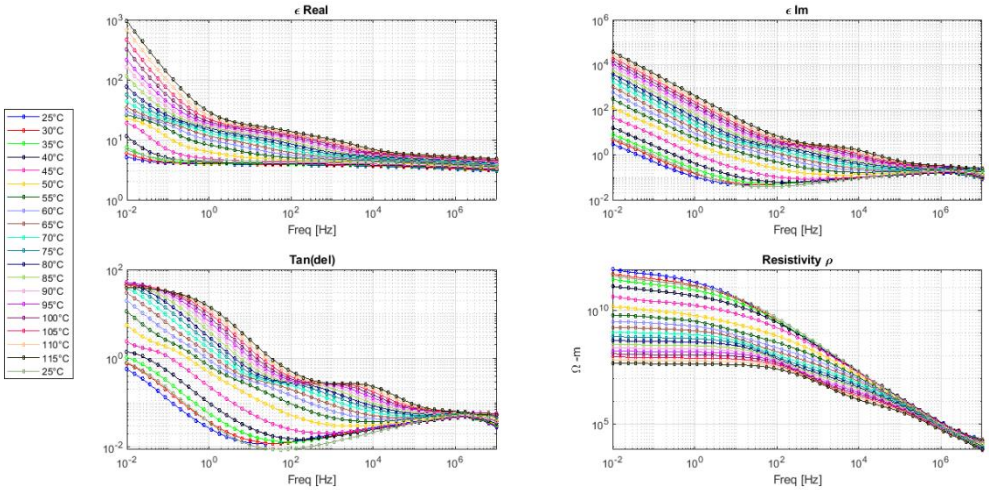

App.A 3 Layfomm60

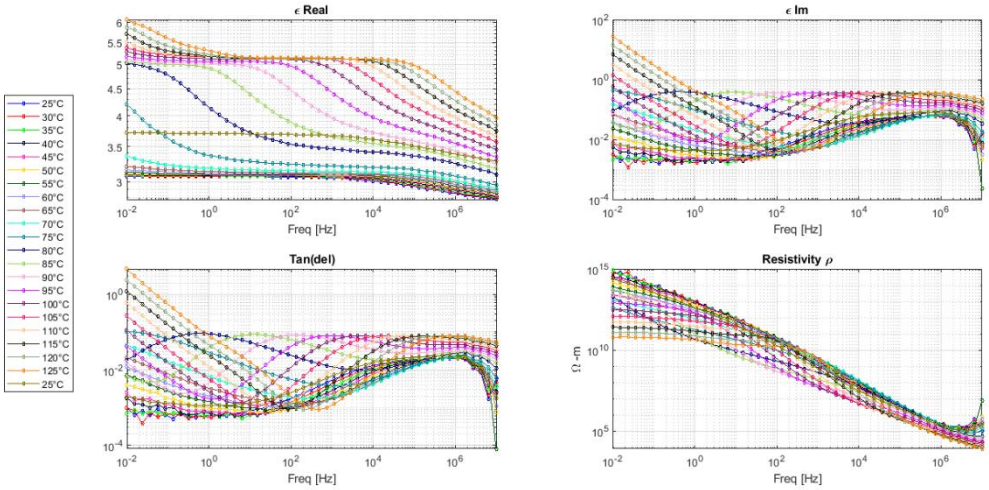

App.A 4 Ryno clear

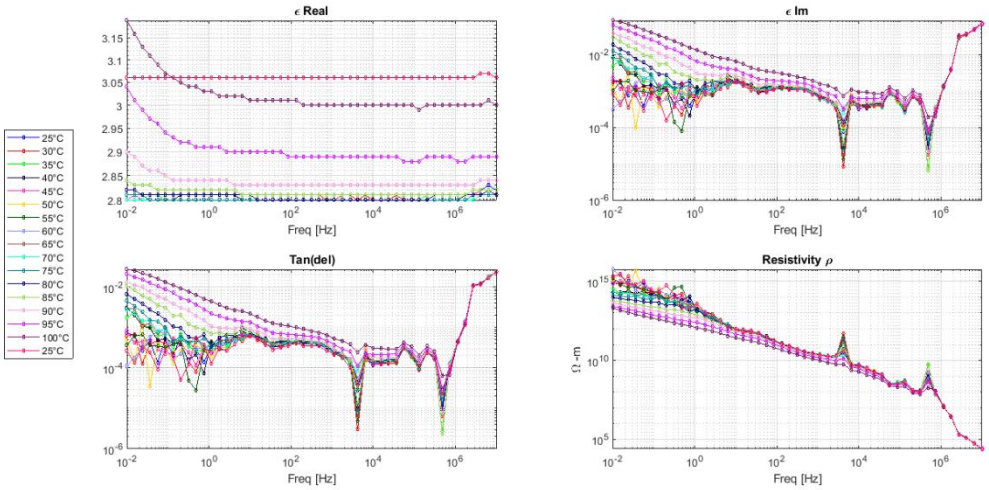

App.A 5 High impact polystyrene

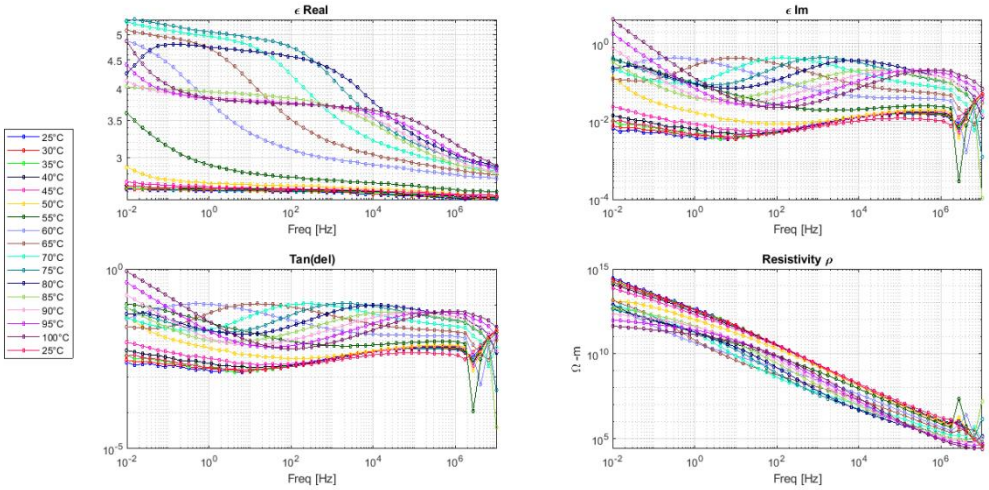

App.A 6 Protopasta PLA white

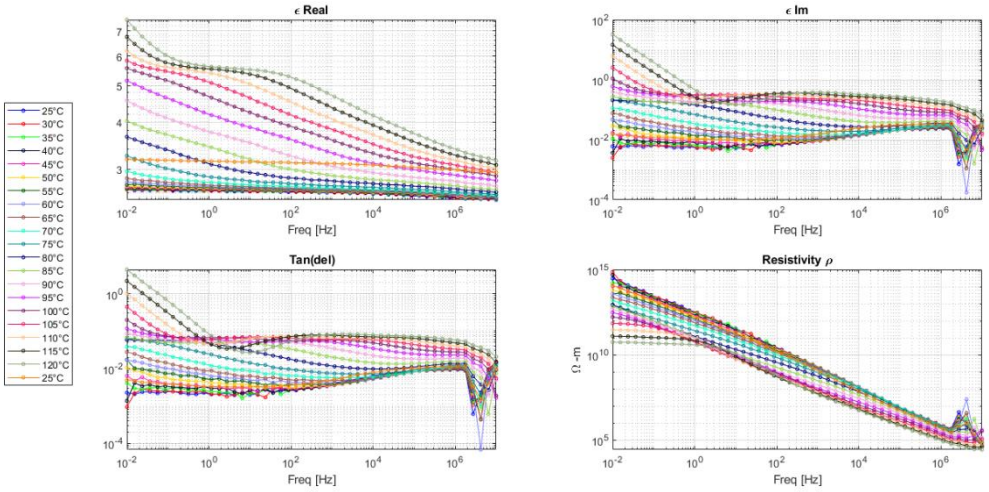

App.A 7 Ultimaker ABS yellow

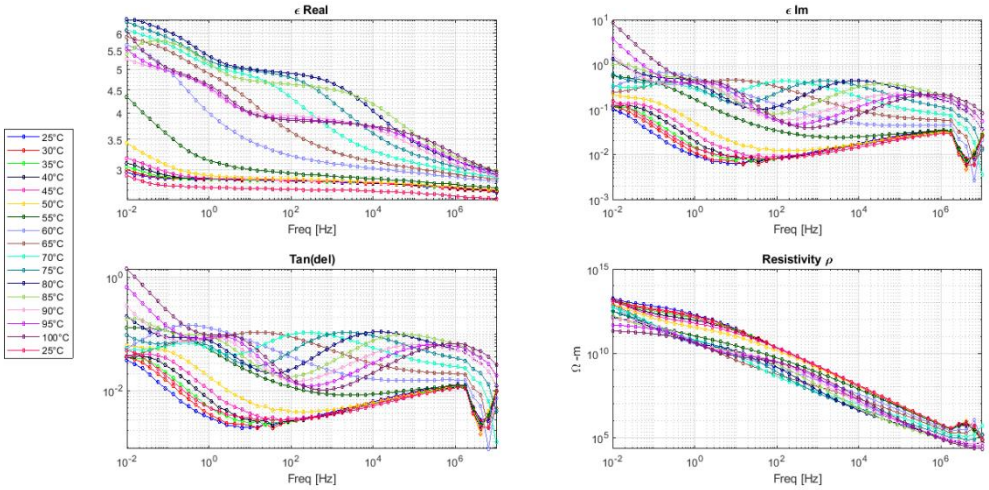

App.A 8 Ultimaker PLA black

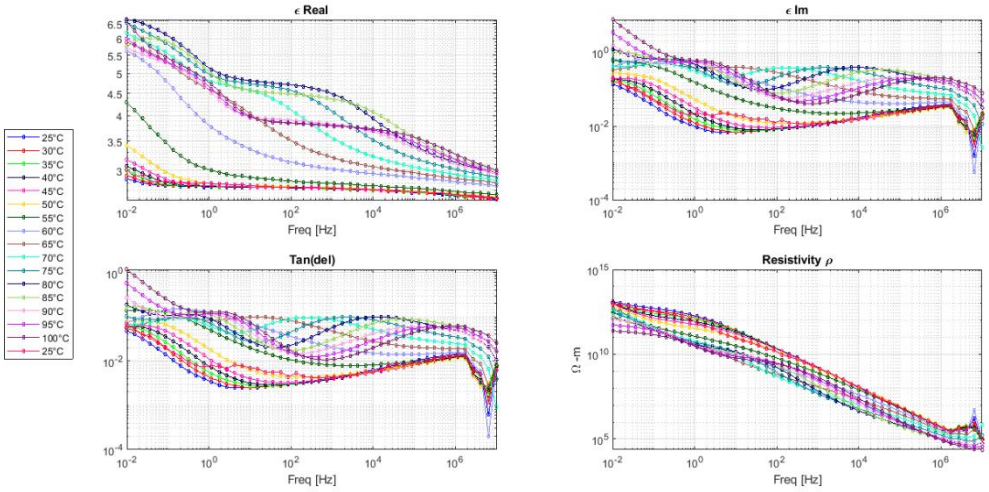

App.A 9 Ultimaker PLA green

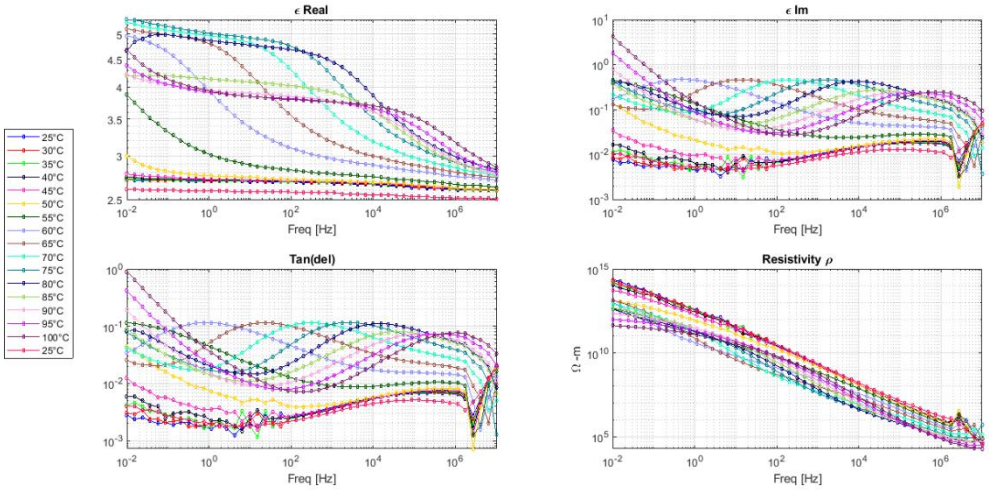

App.A 10 Ultimaker PLA white

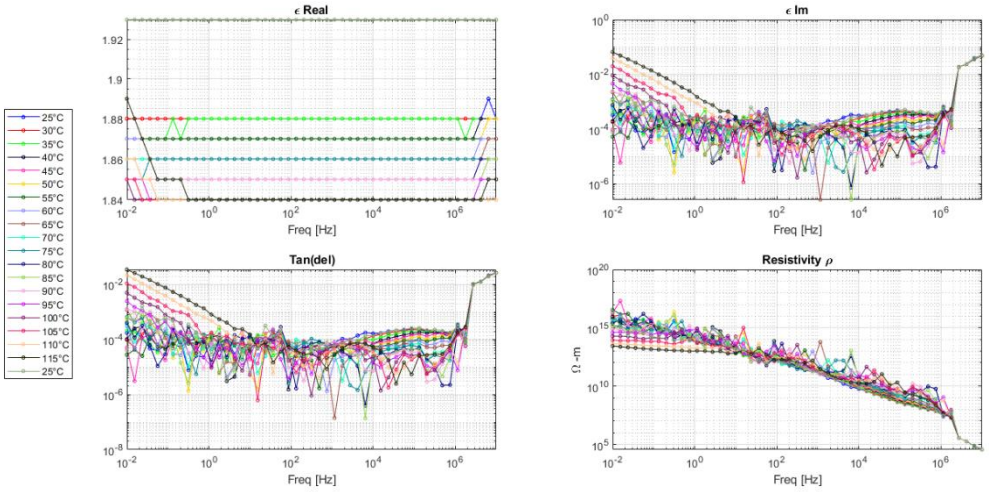

App.A 11 Ultimaker Polypropylene clear

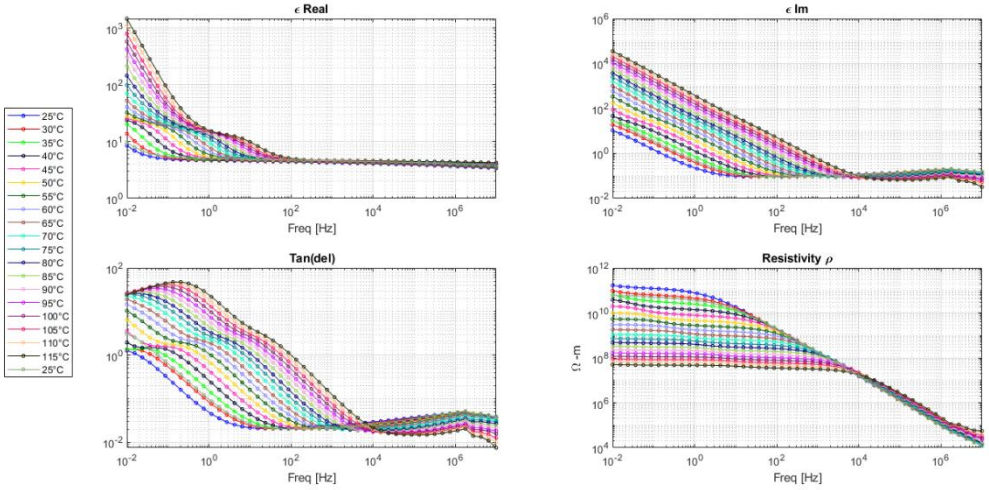

App.A 12 Ultimaker TPU white

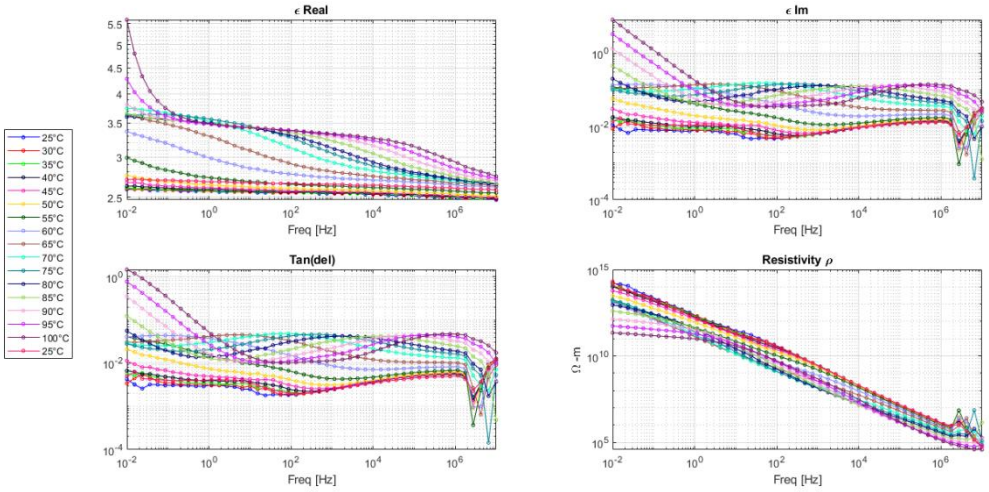

App.A 13 Ultimaker "Natural" PLA, printed with extrusion temp 190°C

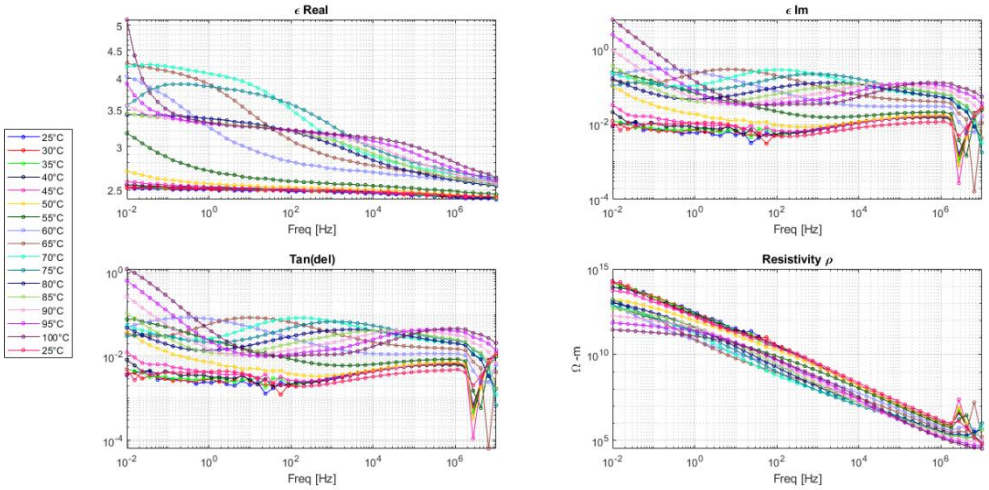

App.A 14 Ultimaker "Natural" PLA, printed with extrusion temp 200°C

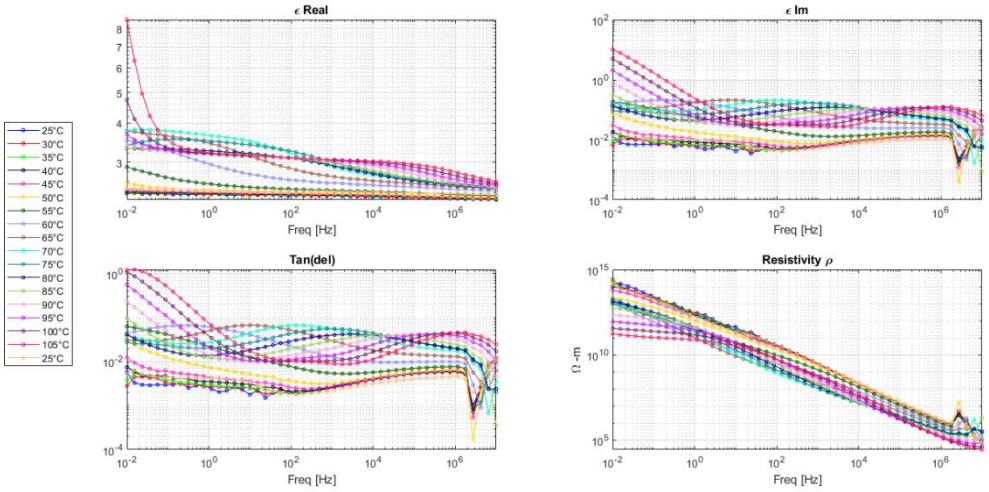

App.A 15 Ultimaker "Natural" PLA, printed with extrusion temp 210°C

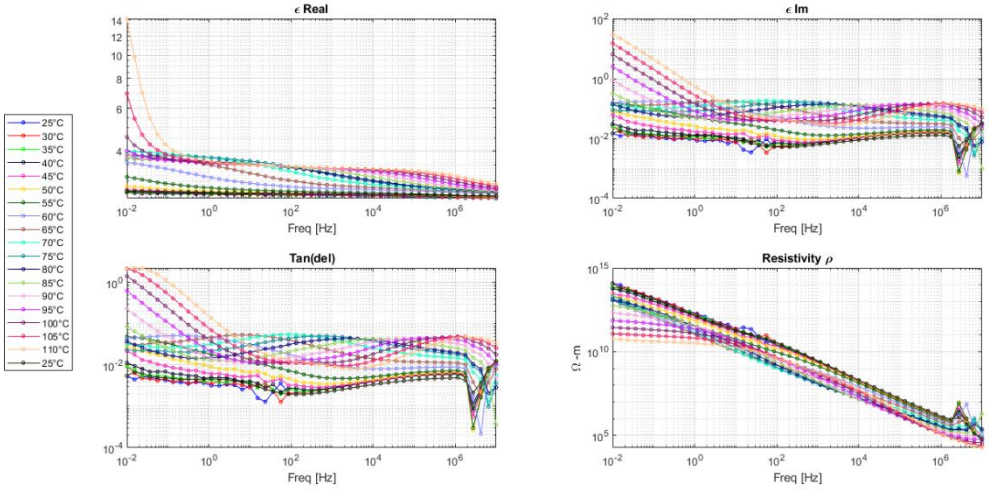

App.A 16 Ultimaker "Natural" PLA, printed with extrusion temp 220°C

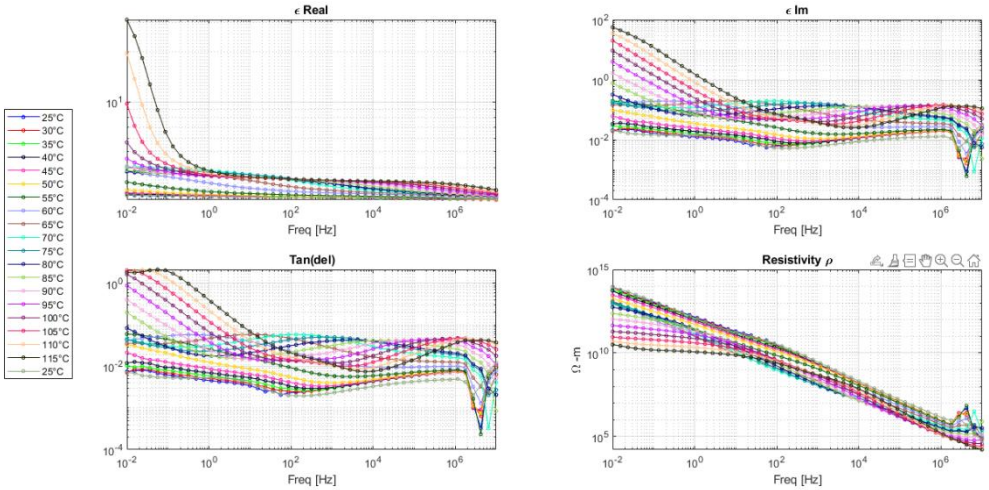

App.A 17 Ultimaker "Natural" PLA, printed with extrusion temp 230°C

Appendix B: Long-term charge decay of 3D printed coupons

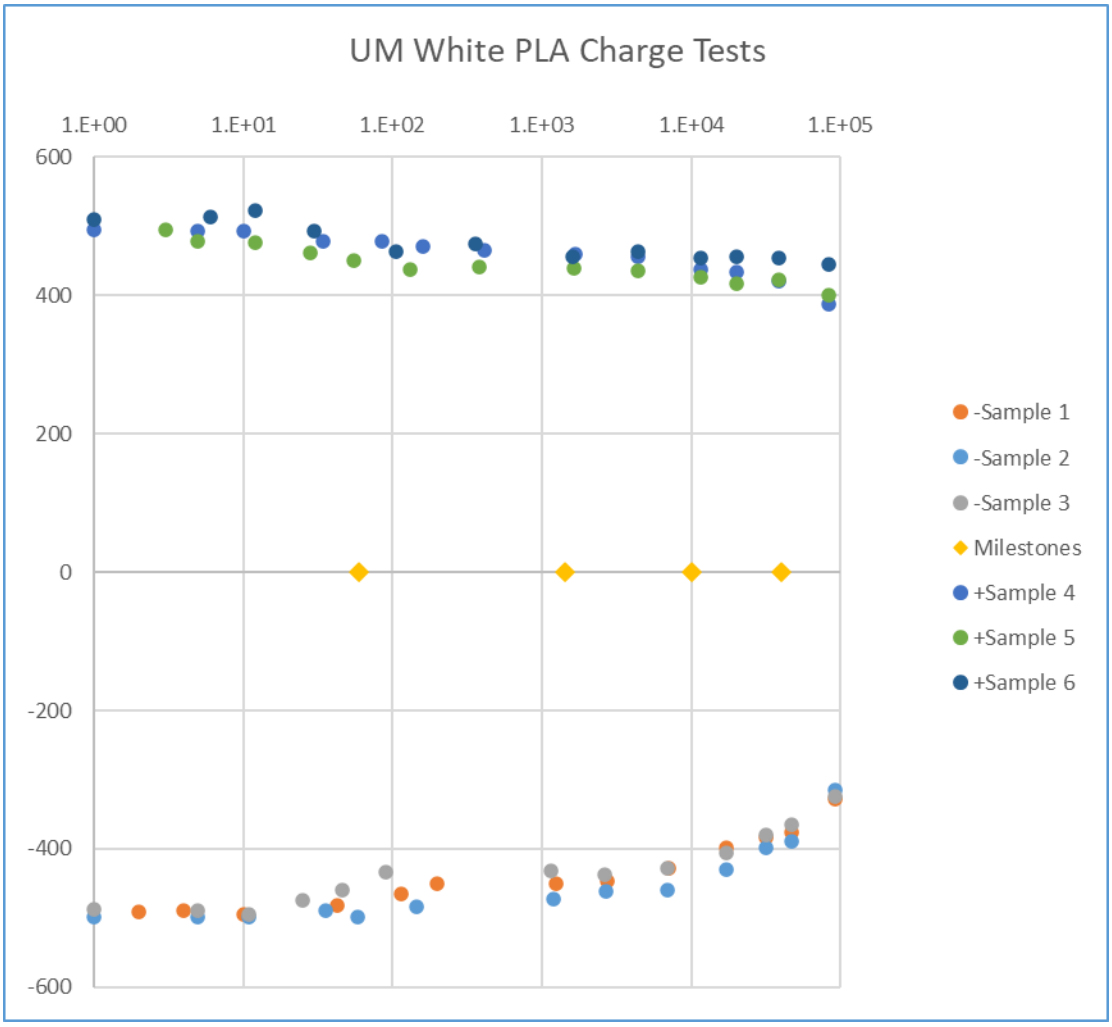

App. B 1 Ultimaker white pla

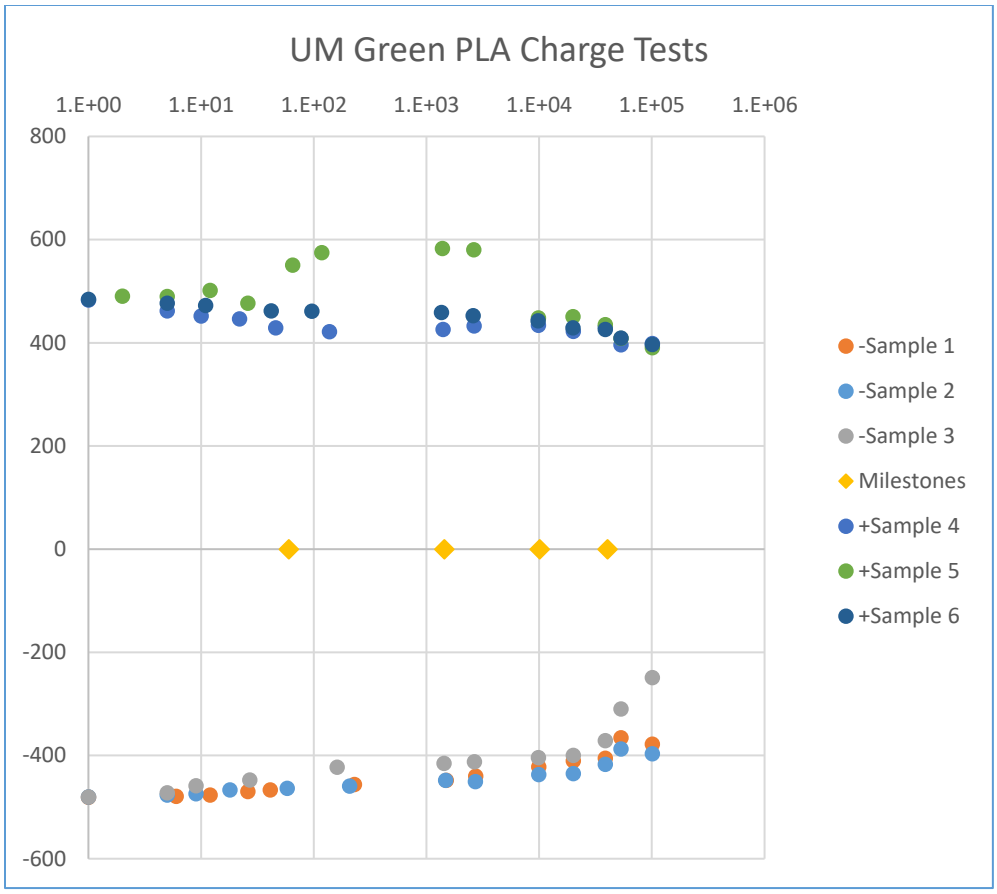

App. B 2 Ultimaker Green PLA

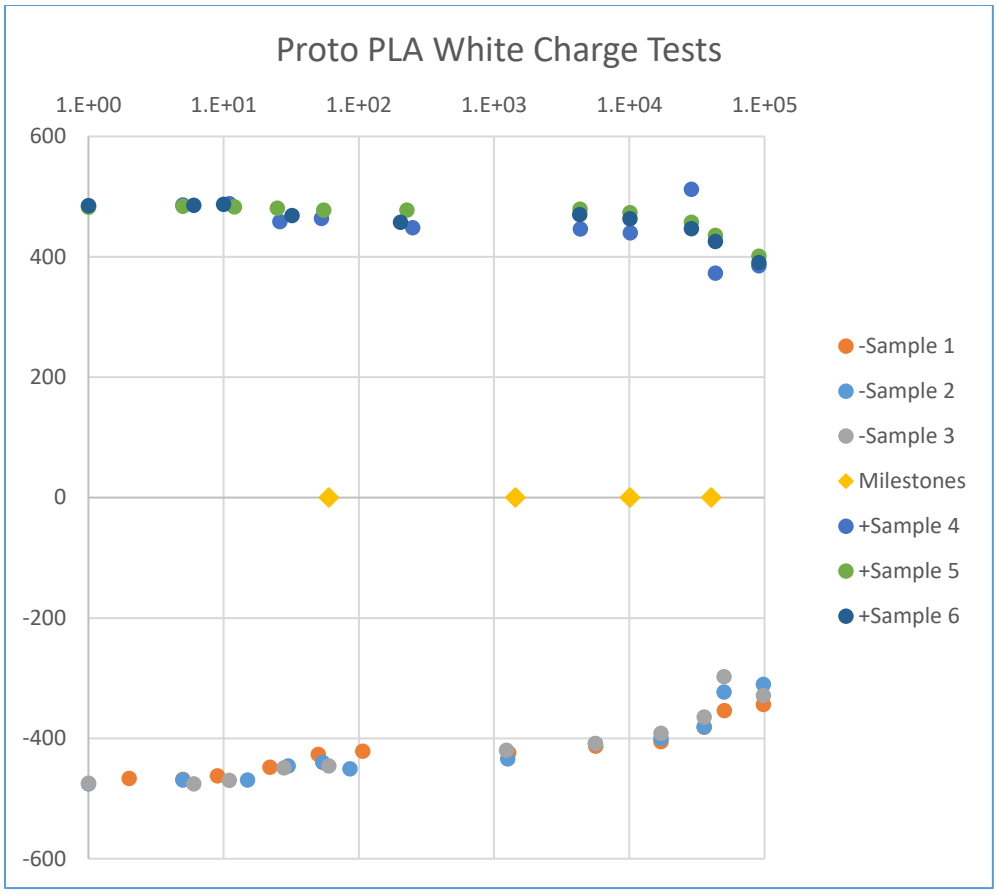

App. B 3 Protopasta white PLA

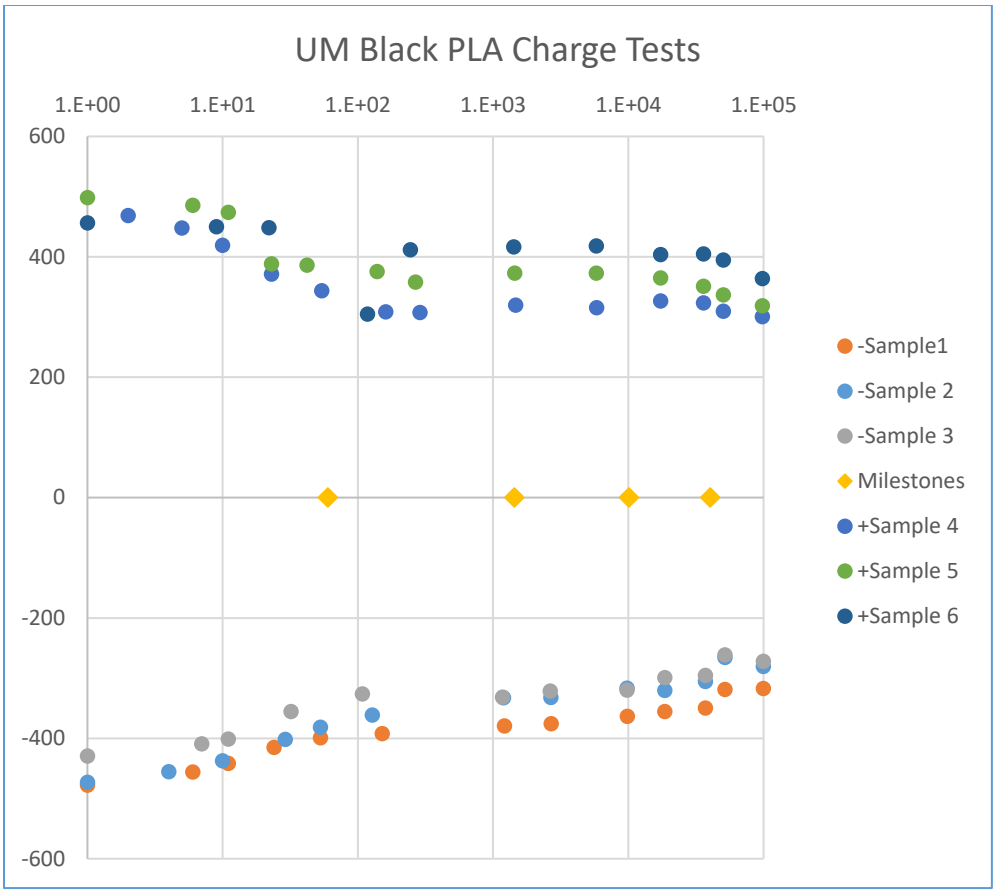

App. B 4 Ultimaker black PLA

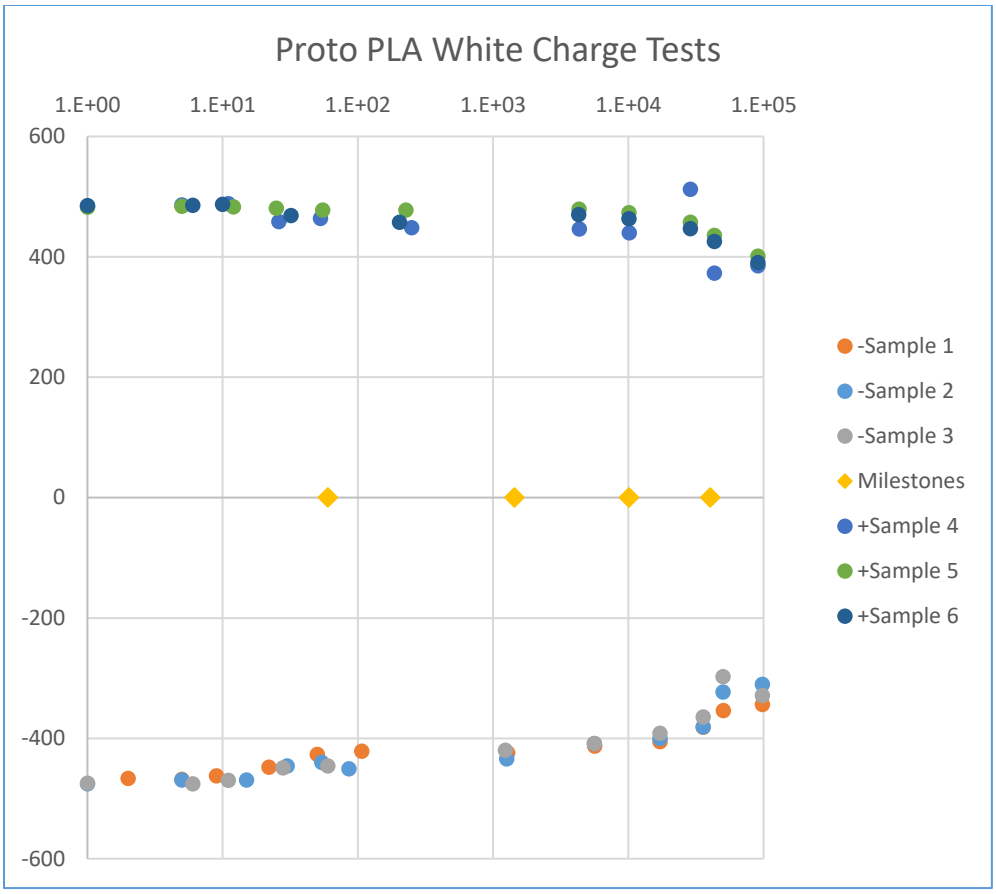
Proto PLA White Charge Tests
1.E+00
1.E+01
1.E+02
1.E+03
1.E+04
1.E+05
600
400
200
0
-200
-400
-600
-Sample 1
-Sample 2
-Sample 3
Milestones
+Sample 4
+Sample 5
+Sample 6

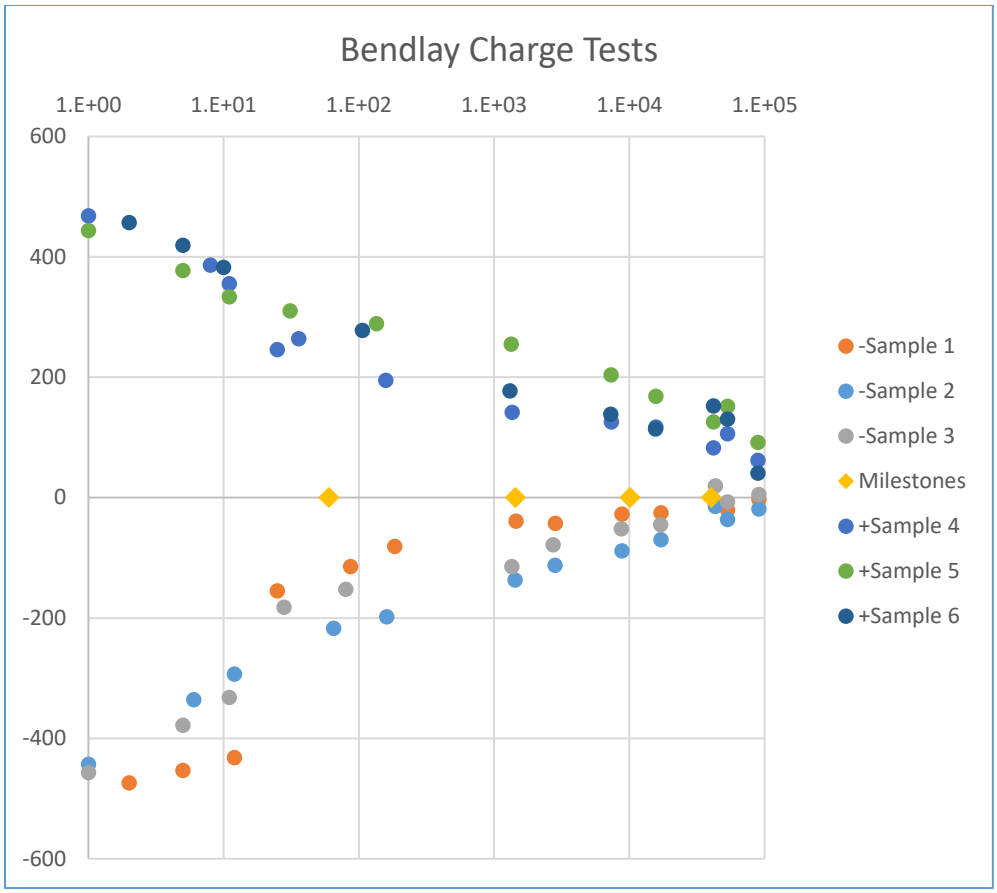
Bendlay Charge Tests
1.E+00
1.E+01
1.E+02
1.E+03
1.E+04
1.E+05
600
400
200
0
-200
-400
-600
-Sample 1
-Sample 2
-Sample 3
Milestones
+Sample 4
+Sample 5
+Sample 6

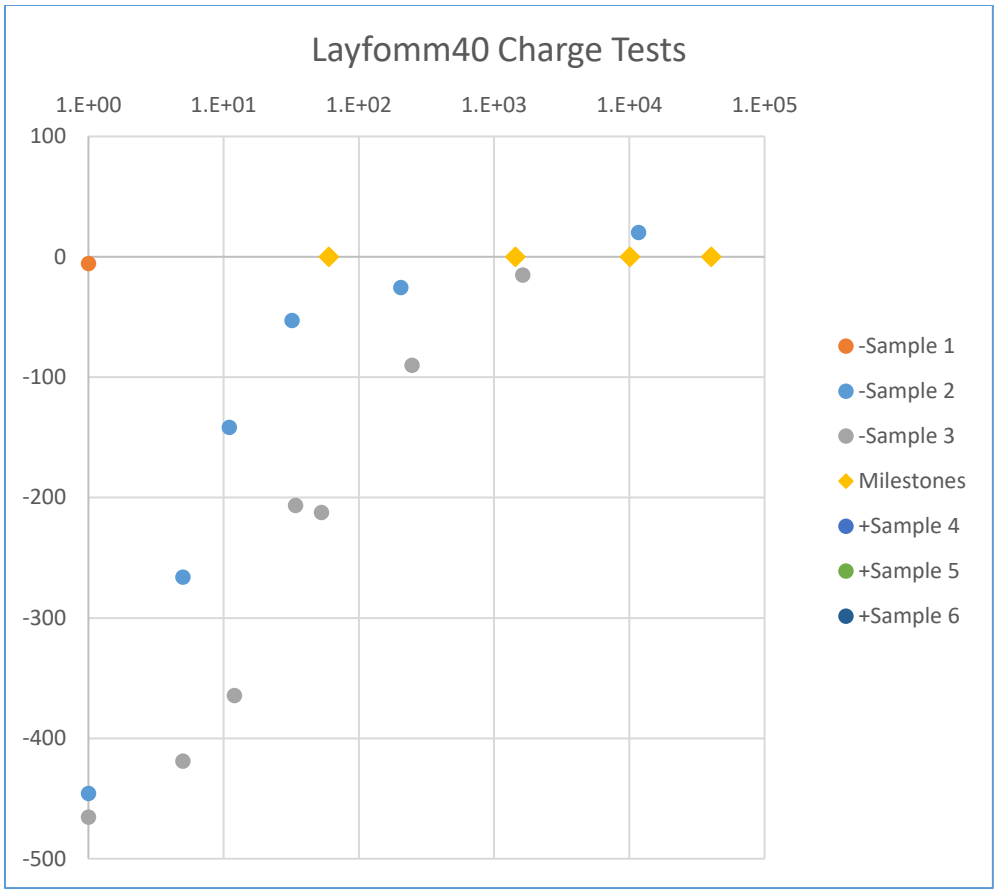
Layfomm40 Charge Tests
1.E+00
1.E+01
1.E+02
1.E+03
1.E+04
1.E+05
100
0
-100
-200
-300
-400
-500
-Sample 1
-Sample 2
-Sample 3
Milestones
+Sample 4
+Sample 5
+Sample 6

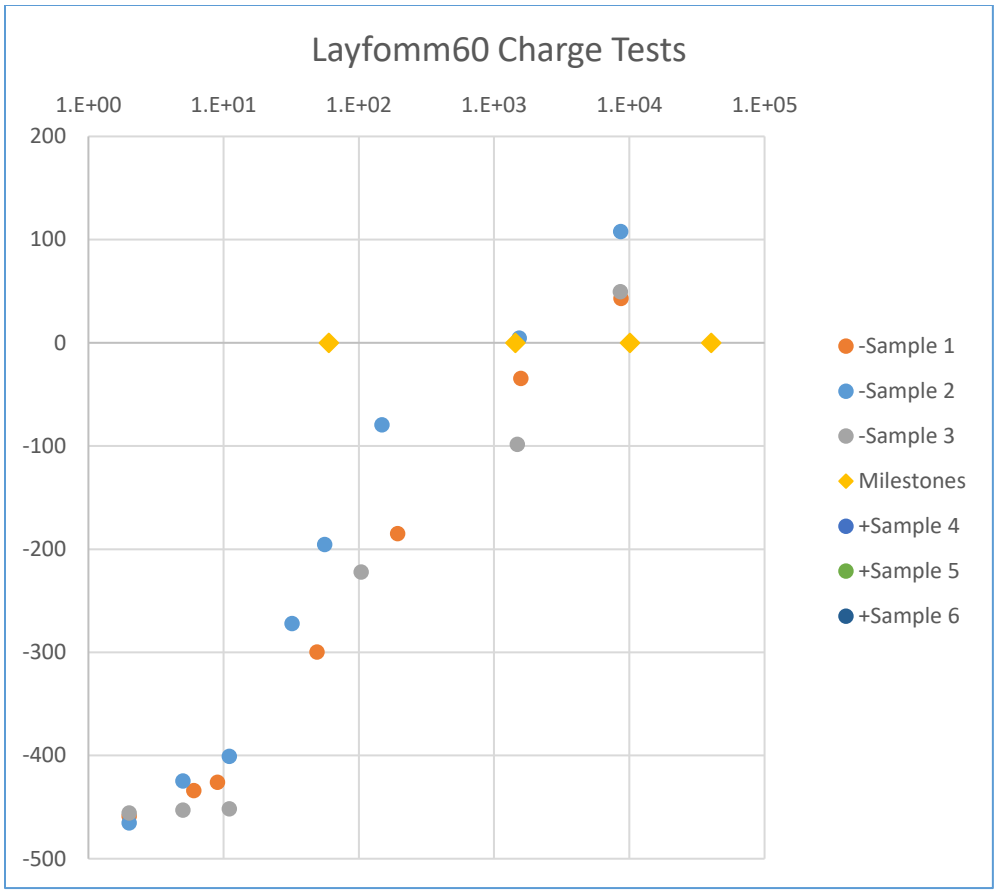
Layfomm60 Charge Tests
1.E+00
1.E+01
1.E+02
1.E+03
1.E+04
1.E+05
200
100
0
-100
-200
-300
-400
-500
-Sample 1
-Sample 2
-Sample 3
Milestones
+Sample 4
+Sample 5
+Sample 6

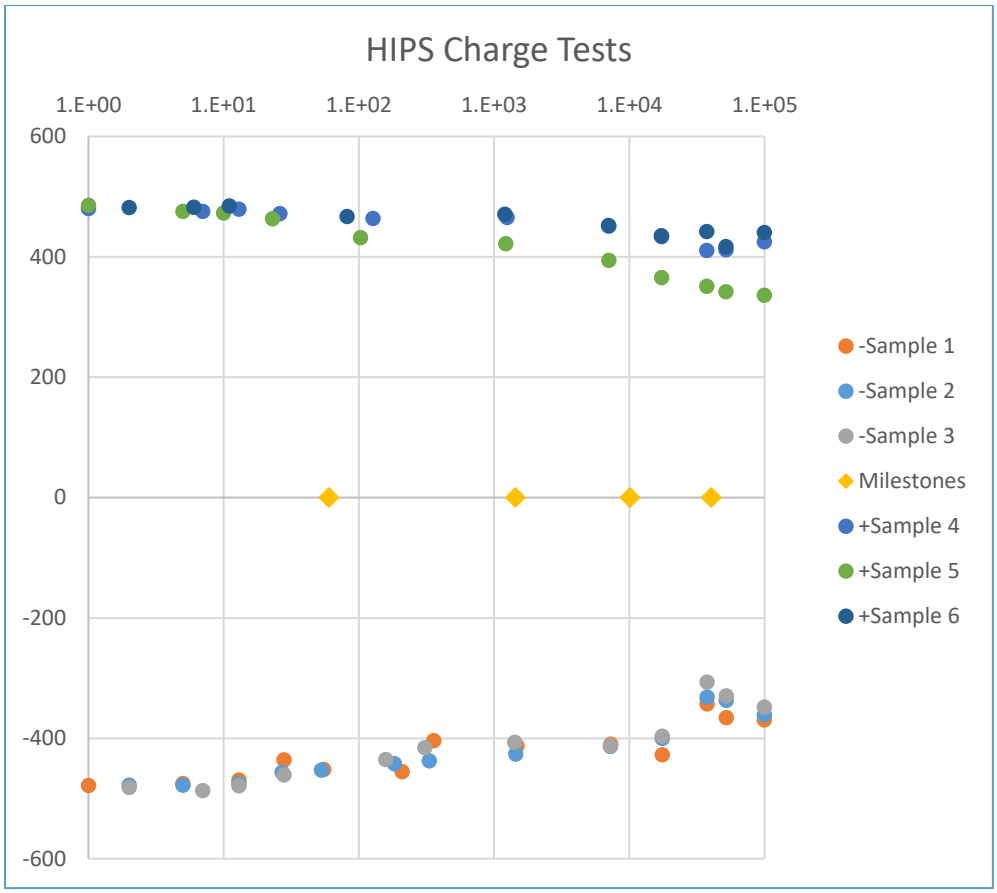
HIPS Charge Tests
1.E+00
1.E+01
1.E+02
1.E+03
1.E+04
1.E+05
600
400
200
0
-200
-400
-600
-Sample 1
-Sample 2
-Sample 3
Milestones
+Sample 4
+Sample 5
+Sample 6

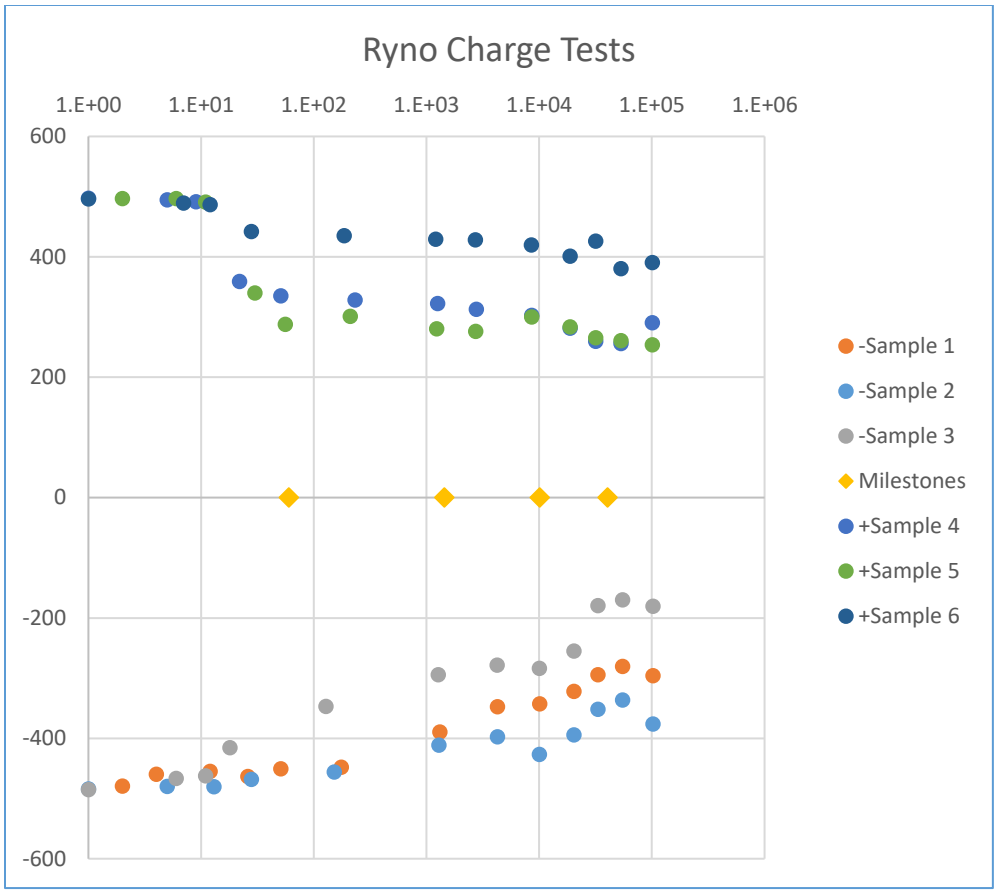
Ryno Charge Tests
1.E+00
1.E+01
1.E+02
1.E+03
1.E+04
1.E+05
1.E+06
600
400
200
0
-200
-400
-600
-Sample 1
-Sample 2
-Sample 3
Milestones
+Sample 4
+Sample 5
+Sample 6

Bibliography

1. Sessler, G.M., *Introduction to Electrets: Principles, equations, experimental techniques*, in *School on Polymers and Composites for Microelectronics and Robotics (PCMR) Lecture Series*. 2004, Institute of Molecular Physics Polish Academy of Sciences.
2. Eguchi, M., *On the permanent electret.* The London, Edinburgh, and Dublin Philosophical Magazine and Journal of Science, 1925. **49**(289): p. 178-192.
3. Swann, W.F.G., *On certain matters pertaining to electrets.* Journal of the Franklin Institute, 1950. **250**(3): p. 219-248.
4. Swann, W.F.G., *Fundamentals in the behavior of electrets.* Journal of the Franklin Institute, 1953. **255**(6): p. 513-530.
5. Gerhard M Sessler, J.E.W., *Electroacoustic transducer*, in *Google Patents*, I. Bell Telephone Laboratories, Editor. 1962, AT&T Corp: United States.
6. Hamdi, O., F. Mighri, and D. Rodrigue, *Piezoelectric cellular polymer films: Fabrication, properties and applications.* AIMS Materials Science, 2018. **5**(5): p. 845-869.
7. Suzuki, Y., *Recent progress in MEMS electret generator for energy harvesting.* IEEJ Transactions on Electrical and Electronic Engineering, 2011. **6**(2): p. 101-111.
8. Pondrom, P., et al., *Energy harvesting with single-layer and stacked piezoelectret films.* IEEE Transactions on Dielectrics and Electrical Insulation, 2015. **22**(3): p. 1470-1476.
9. Fang, P., et al., *Fabrication, Structure Characterization, and Performance Testing of Piezoelectret-Film Sensors for Recording Body Motion.* IEEE Sensors Journal, 2018. **18**(1): p. 401-412.
10. Wang, B., et al., *Ultrasensitive cellular fluorocarbon piezoelectret pressure sensor for self-powered human physiological monitoring.* Nano Energy, 2017. **32**: p. 42-49.
11. Yao, Y., et al., *Bio-Assembled Nanocomposites in Conch Shells Exhibit Giant Electret Hysteresis.* Advanced Materials, 2013. **25**(5): p. 711-718.
12. Wang, J.-J., et al., *Piezoelectric polydimethylsiloxane films for MEMS transducers.* Journal of Micromechanics and Microengineering, 2011. **22**(1): p. 015013.
13. Thakur, R., D. Das, and A. Das, *Electret air filters.* Separation & Purification Reviews, 2013. **42**(2): p. 87-129.
14. Kressmann, R., G.M. Sessler, and P. Gunther, *Space-charge electrets.* IEEE Transactions on Dielectrics and Electrical Insulation, 1996. **3**(5): p. 607-623.
15. Vladimir N. Kestelman, L.S.P., Victor A. Goldade, *Electrets in Engineering Fundamentals and Applications*. 2000: Springer.
16. Sugiyama, T., et al., *SiO2 Electret Generated by Potassium Ions on a Comb-Drive Actuator.* Applied Physics Express, 2011. **4**(11): p. 114103.
17. Minami, T., et al., *SiO2 electret thin films prepared by various deposition methods.* Thin Solid Films, 2003. **426**(1-2): p. 47-52.
18. Tanaka, Y., et al., *Polarization and microstructural effects of ceramic hydroxyapatite electrets.* Journal of Applied Physics, 2010. **107**(1): p. 014107.

19. Klimiec, E., et al., *Increase of Piezoelectric Constant and Thermal Durability of Polypropylene Electret by Introducing SiO2 and Kaolin Filler and Creating a Cellular Structure.* Journal of Electronic Materials, 2015. **44**(7): p. 2283-2291.
20. Hamdi, O., F. Mighri, and D. Rodrigue, *Piezoelectric cellular polymer films: Fabrication, properties and applications.* AIMS Mater. Sci, 2018. **5**: p. 845.
21. Zhukov, S., et al., *Analytical prediction of the piezoelectric d33 response of fluoropolymer arrays with tubular air channels.* Sci Rep, 2018. **8**(1): p. 4597.
22. Zhang, X., et al., *Fluoroethylenepropylene ferroelectrets with patterned microstructure and high, thermally stable piezoelectricity.* Applied Physics A, 2012. **107**(3): p. 621-629.
23. Sakane, Y., Y. Suzuki, and N. Kasagi, *The development of a high-performance perfluorinated polymer electret and its application to micro power generation.* Journal of Micromechanics and Microengineering, 2008. **18**(10).
24. Suzuki, M., et al. *Nano-porous SiO2 electret with high surface potential and high thermal resistance*. 2014. IEEE.
25. S Genter, O.P., *Parylene-C As An Electret Material For Micro Energy Harvesting 2012 Tech.* Dig. PowerMEMS (Atlanta, USA, 2-5 Dec) p, 2012: p. 129-132.
26. Lo, H.-w. and Y.-C. Tai, *Parylene-based electret power generators.* Journal of Micromechanics and Microengineering, 2008. **18**(10): p. 104006.
27. J-J Wang, C.-E.L., S-C Lo, Y-C Su, W Fang. *Composite rubber electret for electromechanical load detection*. in *19th International Conference on Solid-State Sensors, Actuators and Microsystems (TRANSDUCERS)*. 2017. IEEE.
28. Wang, J.-J., et al. *Composite rubber electret with piezoelectric 31 and 33 modes for elastically electromechanical sensors*. in *2015 IEEE SENSORS*. 2015. IEEE.
29. Mirkowska, A., R. Kacprzyk, and K. Rozmaryniewicz, *Piezoelectric Structure With a 3-D Printed Mesh Layer.* IEEE Transactions on Dielectrics and Electrical Insulation, 2022. **29**(3): p. 823-828.
30. Mirkowska, A., *Fabrication and properties of sandwich dielectric structures with piezoelectric response.* IEEE Transactions on Dielectrics and Electrical Insulation, 2024: p. 1-1.
31. Sellami, Y., et al., *Piezoelectret Sensors from Direct 3D-Printing onto Bulk Films*, in *2023 Ieee Sensors*. 2023. p. 1-4.
32. Upadhya, N.P., I.M. Lewis, and A. Mellinger, *Vertically Printed Ferroelectret Microstructures*, in *2023 IEEE Conference on Electrical Insulation and Dielectric Phenomena (CEIDP)*. 2023. p. 1-4.
33. Kierzewski, I., et al., *Adding an electroactive response to 3D printed materials: Printing a piezoelectret.* Additive Manufacturing, 2020. **31**: p. 100963.
34. Boisseau, S., G. Despesse, and B. Ahmed, *Electrostatic Conversion for Vibration Energy Harvesting*, in *Small-Scale Energy Harvesting*. 2012.
35. Gerhard-Multhaupt, R., *Less can be more: holes in polymers lead to a new paradigm of piezoelectric materials for electret transducers.* IEEE Transactions on Dielectrics and Electrical Insulation, 2002. **9**(5): p. 850-859.
36. Kacprzyk, R. and E. Motyl. *Properties of PP-PS double layer electrets*. in *Proceedings of 8th International Symposium on Electrets (ISE 8)*. 1994. IEEE.

37. Paajanen, M., J. Lekkala, and K. Kirjavainen, *ElectroMechanical Film (EMFi) — a new multipurpose electret material.* Sensors and Actuators A: Physical, 2000. **84**(1-2): p. 95-102.
38. Harris, S. and A. Mellinger, *Towards a better understanding of dielectric barrier discharges in ferroelectrets: Paschen breakdown fields in micrometer sized voids.* Journal of Applied Physics, 2014. **115**(16): p. 163302.
39. Go, D.B. and D.A. Pohlman, *A mathematical model of the modified Paschen's curve for breakdown in microscale gaps.* Journal of Applied Physics, 2010. **107**(10): p. 103303.
40. Zhang, G., et al., *Harvesting Energy from Human Activity: Ferroelectric Energy Harvesters for Portable, Implantable, and Biomedical Electronics.* Energy Technology, 2018. **6**(5): p. 791-812.
41. Kachroudi, A., et al., *Micro-structured PDMS piezoelectric enhancement through charging conditions.* Smart Materials and Structures, 2016. **25**(10): p. 105027.
42. Giacometti, J.A., S. Fedosov, and M.M. Costa, *Corona charging of polymers: recent advances on constant current charging.* Brazilian Journal of Physics, 1999. **29**(2): p. 269-279.
43. M Paajanen, M.W., and R Gerhard-Multhaupt, *Understanding the role of the gas in the voids during corona charging of cellular electret films - a way to enhance their piezoelectricity.* J. Phys. D; Apply. Phys., 2001. **34**: p. 2482-2488.
44. Das-Gupta, D.K., *Molecular processes in polymer electrets.* Journal of Electrostatics, 2001. **51-52**: p. 159-166.
45. Gulyakova, A., P. Frubing, and Y. Gorokhovatskiy. *Relaxation processes and electret properties of titanium-dioxide filled high-impact polystyrene films*. 2011. IEEE.
46. Gulyakova, A.A., et al., *Relaxation processes determining the electret stability of high-impact polystyrene/titanium-dioxide composite films.* IEEE Transactions on Dielectrics and Electrical Insulation, 2017. **24**(4): p. 2541-2548.
47. Mellinger, A., *Dielectric resonance spectroscopy: a versatile tool in the quest for better piezoelectric polymers.* IEEE Transactions on Dielectrics and Electrical Insulation, 2003. **10**(5): p. 842-861.
48. Thyssen, A., K. Almdal, and E.V. Thomsen, *Electret stability related to the crystallinity in polypropylene.* IEEE Transactions on Dielectrics and Electrical Insulation, 2017. **24**(5): p. 3038-3046.
49. Thyssen, A., K. Almdal, and E.V. Thomsen, *Electret stability related to spherulites in polypropylene.* IEEE Transactions on Dielectrics and Electrical Insulation, 2015. **22**(5): p. 2858-2863.
50. Xiao, H., et al., *Study on correlation of filtration performance and charge behavior and crystalline structure for melt-blown polypropylene electret fabrics.* Journal of Applied Polymer Science, 2015. **132**(47): p. n/a-n/a.
51. Lorenzo, A.T., et al., *DSC isothermal polymer crystallization kinetics measurements and the use of the Avrami equation to fit the data: Guidelines to avoid common problems.* Polymer Testing, 2007. **26**(2): p. 222-231.
52. Llovera, P., et al., *Measurements of electrostatic potentials and electric fields in some industrial applications: Basic principles.* Journal of Electrostatics, 2009. **67**(2-3): p. 457-461.

53. Kim, S., et al., *Effect of end group of amorphous perfluoro-polymer electrets on electron trapping.* Science and Technology of Advanced Materials, 2018. **19**(1): p. 486-494.
54. Qiu, X., W. Wirges, and R. Gerhard, *Polarization and Hysteresis in Tubular-Channel Fluoroethylenepropylene-Copolymer Ferroelectrets.* Ferroelectrics, 2014. **472**(1): p. 100-109.
55. Qiu, X., W. Wirges, and R. Gerhard, *Thermal poling of ferroelectrets: How does the gas temperature influence dielectric barrier discharges in cavities?* Applied Physics Letters, 2016. **108**(25): p. 252901.
56. Qiu, X., *Significant enhancement of the charging efficiency in the cavities of ferroelectrets through gas exchange during charging.* Applied Physics Letters, 2016. **109**(22): p. 222903.
57. Joysey, W.D. and A. Mellinger. *Ferroelectrets Filled with a High Breakdown-Strength Gas*. in *2018 IEEE Conference on Electrical Insulation and Dielectric Phenomena (CEIDP)*. 2018. IEEE.
58. Qiu, X., *Patterned piezo-, pyro-, and ferroelectricity of poled polymer electrets.* Journal of Applied Physics, 2010. **108**(1): p. 011101.
59. Hamdi, O., F. Mighri, and D. Rodrigue, *Optimization of the cellular morphology of biaxially stretched thin polyethylene foams produced by extrusion film blowing.* Cellular Polymers, 2018. **37**(4-6): p. 153-168.
60. M Paajanen, H.M., and J Raukola. *Gas diffusion expansion increased thickness and enhanced electromechanical response of cellular polymer electret films*. in *11th International Symposium on Electrets*. 2002. Melbourne, Victoria, Australia: IEEE.
61. Luo, Z., D. Zhu, and S.P. Beeby, *Multilayer ferroelectret-based energy harvesting insole.* Journal of Physics: Conference Series, 2015. **660**: p. 012118.
62. Zhukov, S., et al., *Tubular fluoropolymer arrays with high piezoelectric response.* Smart Materials and Structures, 2018. **27**(1): p. 015010.
63. Wang, F. and O. Hansen, *Invisible Surface Charge Pattern on Inorganic Electrets.* IEEE Electron Device Letters, 2013. **34**(8): p. 1047-1049.
64. Li, T., et al., *Exploiting negative Poisson's ratio to design 3D-printed composites with enhanced mechanical properties.* Materials & Design, 2018. **142**: p. 247-258.
65. MacDonald, E. and R. Wicker, *Multiprocess 3D printing for increasing component functionality.* Science, 2016. **353**(6307).
66. Shi, J., D. Zhu, and S.P. Beeby, *An investigation of PDMS structures for optimized ferroelectret performance.* Journal of Physics: Conference Series, 2014. **557**: p. 012104.
67. Shi, J., et al., *Optimization of a PDMS structure for energy harvesting under compressive forces.* Journal of Physics: Conference Series, 2015. **660**: p. 012041.
68. Kacprzyk, R. and A. Mirkowska. *Contemporary inhomogeneous piezo-active dielectric structures*. in *2018 Innovative Materials and Technologies in Electrical Engineering (i-MITEL)*. 2018. IEEE.
69. Peterson, A.M., *Review of acrylonitrile butadiene styrene in fused filament fabrication: A plastics engineering-focused perspective.* Additive Manufacturing, 2019. **27**: p. 363-371.
70. Assagra, Y.A.O., et al., *Piezoelectrets with well-defined cavities produced from 3D-printed acrylonitrile butadiene styrene structures.* Electronics Letters, 2015. **51**(24): p. 2028-2030.

71. Assagra, Y.A.O., et al. *Well-defined piezoelectrets fabricated with 3D printing technology*. in *2016 IEEE International Conference on Dielectrics (ICD)*. 2016. IEEE.
72. Palitó, T.T.C., et al., *Hydrophone based on 3D printed polypropylene (PP) piezoelectret.* Electronics Letters, 2019. **55**(4): p. 203-204.
73. Mo, C., R. Yin, and J.R. Raney, *Direct ink writing of tough, stretchable silicone composites.* Soft Matter, 2022. **18**(38): p. 7341-7347.
74. Frese, T., et al., *Electret Properties of Polyetherimides: Influence of Water Content and Comparison with Other High-Temperature Polymer Films.* 2007. **292**(5): p. 582-587.
75. Guzhova, A.A., et al., *Improvement of polylactic acid electret properties by addition of fine barium titanate.* Journal of Electrostatics, 2016. **79**: p. 1-6.
76. Wittbrodt, B. and J.M. Pearce, *The effects of PLA color on material properties of 3-D printed components.* Additive Manufacturing, 2015. **8**: p. 110-116.
77. Yang, C., et al., *Influence of thermal processing conditions in 3D printing on the crystallinity and mechanical properties of PEEK material.* Journal of Materials Processing Technology, 2017. **248**: p. 1-7.
78. Liao, Y., et al., *Effect of Porosity and Crystallinity on 3D Printed PLA Properties.* Polymers, 2019. **11**(9): p. 1487.
79. Galikhanov, E., et al., *Study of polylactic acid electret by dielectric spectroscopy*. 2016.
80. Galikhanov, M., et al., *Study of Electret State in Epoxyamine Polymers by Dielectric Spectroscopy.* Journal of Electronic Materials, 2019. **48**(7): p. 4473-4477.
81. Kilic, A., E. Shim, and B. Pourdeyhimi, *Effect of annealing on charging properties of electret fibers.* The Journal of The Textile Institute, 2016. **108**(6): p. 987-991.
82. Kachroudi, A., et al., *Annealing for the improvement of the capabilities of parylene C as electret.* Journal of Applied Polymer Science, 2019. **136**(1): p. 46908.
83. Zhu, H., et al., *Wood-Derived Materials for Green Electronics, Biological Devices, and Energy Applications.* Chem Rev, 2016. **116**(16): p. 9305-74.
84. Li, T., et al., *Scalable and Highly Efficient Mesoporous Wood-Based Solar Steam Generation Device: Localized Heat, Rapid Water Transport.* Advanced Functional Materials, 2018. **28**(16): p. 1707134.
85. Qiu, X., et al., *Direct hysteresis measurements on ferroelectret films by means of a modified Sawyer–Tower circuit.* Journal of Applied Physics, 2013. **113**(22): p. 224106.
86. SIMPSON, W.T., *PREDICTING EQUILIBRIUM MOISTURE CONTENT OF WOOD BY MATHEMATICAL MODELS*, in *Reprinted from WOOD AND FIBER Vol. 5, No. 1, Spring 1973 pp. 41-49*. 1973: https://www.fpl.fs.fed.us/.
87. *<Notingher et al_dielectric properties of wood polymer composites_MATERIALE PLASTICE_2010.pdf>.*
88. Li, T., et al., *Developing fibrillated cellulose as a sustainable technological material.* Nature, 2021. **590**(7844): p. 47-56.
89. Sappati, K.K. and S. Bhadra, *Piezoelectric Polymer and Paper Substrates: A Review.* Sensors (Basel), 2018. **18**(11).